"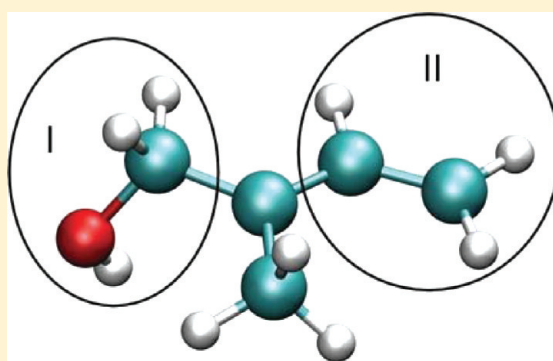Pump−Probe" Atom-Centered Density Matrix Propagation Studies To Gauge Anharmonicity and Energy Repartitioning in Atmospheric Reactive Adducts: Case Study of the OH + Isoprene and OH + Butadiene Reaction Intermediates

Alexander B. Pacheco,[†] Scott M. Dietrick,[†] Philip S. Stevens,[†,‡] and Srinivasan S. Iyengar*[,†,§]

[†]Department of Chemistry, [‡]Center for Research in Environmental Science, School of Public and Environmental Affairs, and [§]Department of Physics, Indiana University, Bloomington, Indiana 47405, United States
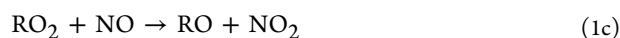
ABSTRACT: Time-resolved "pump−probe" ab initio molecular dynamics studies are constructed to probe the stability of reaction intermediates, the mechanism of energy transfer, and energy repartitioning, for moieties involved during the interaction of volatile organic compunds with hydroxyl radical. These systems are of prime importance in the atmosphere. Specifically, the stability of reaction intermediates of hydroxyl radical adducts to isoprene and butadiene molecules is used as a case study to develop novel computational techniques involving "pump−probe" ab initio molecular dynamics. Starting with the various possible hydroxyl radical adducts to isoprene and butadiene, select vibrational modes of each of the adducts are populated with excess energy to mimic the initial conditions of an experiment. The flow of energy into the remaining modes is then probed by subjecting the excited adducts to ab initio molecular dynamics simulations. It is found that the stability of the adducts arises directly due to the anhormonically driven coupling of the modes to facilitate repartitioning of the excess vibrational energy. This kind of vibrational repartitioning has a critical influence on the energy density.

1. INTRODUCTION

The hydroxyl (OH) and peroxy radicals (HO_2 and RO_2) play a central role in the chemistry of the atmosphere. Through the oxidation of volatile organic compounds (VOCs), the OH radical initiates reactions that lead to the production of ozone and secondary aerosols in the atmosphere. Most of these reactions convert OH to both HO_2 and organic peroxy radicals (RO_2), which in the presence of nitrogen oxides (NO_x) typically found in urban areas are converted back to OH, resulting in a fast cycling of radicals that leads to the formation of ozone, the primary component of photochemical smog:
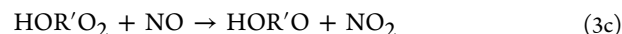
$$OH + VOC \rightarrow R + H_2O \tag{1a}$$

$$R + O_2 \rightarrow RO_2 \tag{1b}$$

$$RO_2 + NO \rightarrow RO + NO_2 \tag{1c}$$

$$\rightarrow RONO_2 \tag{1d}$$

$$HO_2 + NO \rightarrow OH + NO_2 \tag{1e}$$

$$NO_2 + h\nu \xrightarrow{O_2} NO + O_3 \tag{1f}$$

The situation is different on the regional scale, where ozone production tends to be limited by the lower concentration of NO_x.[1]

This results in competing self- and cross-reactions of peroxy radicals, thus terminating the radical chain according to

$$RO_2 + RO_2 \rightarrow 2RO + O_2 \tag{2a}$$

$$\rightarrow ROH + R'(O) + O_2 \tag{2b}$$

$$HO_2 + RO_2 \rightarrow ROOH + O_2 \tag{2c}$$
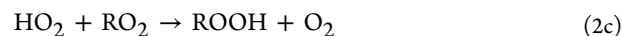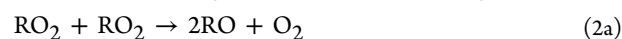
Measurements of OH and HO_2 can provide a critical test of our understanding of the fast photochemistry of these regions of the atmosphere.[2] However, many of these measurements show serious discrepancies with modeled concentrations of OH and HO_2, especially in forest environments dominated by isoprene emissions, bringing into question our understanding of the fast photochemistry of the troposphere, and specifically the atmospheric chemistry of isoprene.[2−5] Unlike the OH-initiated oxidation of alkanes (reaction 1a), the OH-initiated reactions of unsaturated VOCs such as isoprene involve OH addition to one of the carbon−carbon double bonds, resulting in the formation of hydroxy peroxy radicals:

$$OH + VOC \rightarrow R'OH(adduct) \tag{3a}$$

$$R'OH + O_2 \rightarrow HOR'O_2 \tag{3b}$$

$$HOR'O_2 + NO \rightarrow HOR'O + NO_2 \tag{3c}$$

To improve our understanding of the chemical mechanism of the OH-initiated oxidation of isoprene and other unsaturated VOCs, there have been several experimental measurements on the kinetics and mechanism of the OH-initiated oxidation of unsaturated VOCs such as isoprene and butadiene.[6] For such cases, it has recently been proposed[7] that several hydrogen-bonded peroxyl radicals could be formed as intermediates in the OH-initiated oxidation of isoprene. Furthermore, rearrangements of these peroxy radicals, through hydride, proton, or hydrogen atom shifts, followed by unimolecular decomposition or reaction with HO_2 can give rise to additional products including HO_x radicals, aldehydes, and peroxols. Factors that govern the stability of such hydrogen-bonded systems may include enthalpic as well as entropic contributions, since some of these involve formation of six- and eight-membered hydrogen-bonded rings. In addition, the influence of water on the stability of these hydrogen-bonded intermediates may also be critical, and this aspect has been computationally examined in refs 8 and 9. In this regard also see refs 10−23.

The importance of the proposed peroxy radical reactions[7] in the atmosphere depends on the rate of these peroxy radical isomerization reactions relative to the self- and cross-reactions of these peroxy radicals. Facilitating rate constant calculation studies for such complex systems is generally performed using the Rice−Ramsperger−Kassel−Marcus (RRKM) theory to compute unimolecular reaction rates. Computations on the vibrational partition function required in the RRKM rate expression are generally performed within the harmonic approximation. Here the harmonic frequencies obtained at optimized nuclear configurations or transition states provide an approximation to the vibrational density of states. These results are also used as corrections for nuclear zero-point motion. This approach is, however, not adequate for systems that demonstrate soft modes, such as hydrogen bonds,[6,8,9,19,21−27] and the effect of nuclear motion beyond the harmonic approximation must be considered. When hydrogen bonds facilitate reactions, shifts in transition states have been noted,[28] and these shifts are absent when the energies are computed within the harmonic approximation. These contributions are in addition to any anharmonicity contributions that may arise as a result of the floppy hydrogen-bond modes. In refs 29 and 30, the limitations mentioned above are partially surmounted through the use of Miller's semiclassical rate theory.[31] The general idea in refs 29 and 30 is to obtain a second-order perturbation theory based fit to the potential surface[32,33] through detailed electronic structure calculations. Following this, the vibrational density of states correction is obtained through a sum over states algorithm.[29] Our studies here differ through the use of ab initio molecular dynamics (AIMD) to compute approximations to the (anharmonic) potential surface. Through recent studies[8,9,19,21,23−26,34] the use of AIMD to accurately represent vibrational properties of hydrogen-bonded systems, in agreement with experiment, has been demonstrated. (Also see Appendix A in ref 9 for a brief overview.) These studies have included a detailed examination of H/D isotope effects including their dependence on temperature.[25,26] In this paper we further utilized these techniques to examine the following: (a) the role of anharmonicity on the energy density and (b) the effect of preparation of the system where the initial vibrational-state population is skewed toward a nonequilibrium situation. Toward assessing the effect of the latter, we introduce a new technique called "pump−probe" ab initio molecular dynamics. The effect of water on the energy density may also

be critical, and this aspect is studied in ref 9. These studies focus on the initial step of the OH + isoprene reaction leading to the formation of the hydroxyl−isoprene alkyl radicals. Although the atmospheric fate of these hydroxyl alkyl radicals is predominantly reaction with O_2 to form peroxy radicals, the results of this study will be useful to compare to studies of isoprene-based peroxy radicals, which will be a topic of a future publication.

The paper is organized as follows:. In section 2, the simulation strategies are described. Specifically, the dynamics methodology is briefly summarized in section 2.1 and approaches to utilize the trajectory data to construct energy densities are summarized in section 2.2. The "pump−probe" technique used to tailor the dynamics is essentially a modification of initial conditions for dynamics, and this aspect is discussed in section 3.2 along with the results from these dynamics simulations. All computational results are provided in section 3, while conclusions are given in section 4.

2. THEORETICAL METHODS

The AIMD simulations involve performing quantum chemical calculations "on-the-fly" to obtain the potential energy and nuclear forces.[35−44] The simulations conducted here are similar to those discussed in refs 6, 8, 19−22, 25, and 26. The atom-centered density matrix propagation (ADMP),[22,23,34,40,45−49] AIMD technique, as implemented within the Gaussian series of electronic structure codes,[50] has been employed in these studies. This method is briefly reviewed in Appendix A of ref 9 with further details on the methodological aspects in refs 40, 45−49, and 51 and applications in refs 6, 8, 19−23, 34, 46, 51, and 52. However, for reader convenience, a brief review is also presented here in section 2.1.

All systems considered here are treated as gas-phase clusters to remain consistent with the experimental work.[6] A fictitious mass-tensor scale value of 0.1 amu·bohr^2 ($\approx$180 au) and a time step of 0.25 fs was used for ADMP. The AIMD simulations conducted here are microcanonical (that is, constant number of particles, volume, and total energy and hence depicted as NVE), with acceptable fluctuations in the internal temperature. (Simulation details are provided in Table 1 with associated discussion in section 3.2.) All nuclei are treated classically. Since time-correlation functions involving nuclear velocities and molecular dipoles (see below) are utilized to obtain vibrational energy distributions, a constant energy simulation with an associated conservative Hamiltonian corresponding to the real system is critical. [These constant energy simulations however also have approximately fixed temperatures, with acceptable fluctuations as noted above.] The total energy in these simulations was well-conserved in our simulations. The total angular momentum of the classical nuclear system was also well-conserved (with initial conditions corresponding to $J = 0$), and residual angular forces, resulting from finite numerical precision, were projected out during the dynamics process.[26] A body-fixed $3N$-dimensional Cartesian coordinate system positioned at the center of mass, conserved all through the dynamics, was used to represent nuclear positions and momenta.

As noted above, the ADMP method is briefly reviewed in section 2.1, following which methods to compute vibrational energy distribution are discussed in section 2.2. The "pump−probe" technique used to tailor the dynamics is essentially a modification of initial conditions in ADMP, and this aspect is discussed in section 3.2 along with the results from these dynamics simulations.

B

dx.doi.org/10.1021/jp212330e | J. Phys. Chem. A XXXX, XXX, XXX−XXX

Table 1. AIMD Simulation Parameters for the Hydroxy Isoprene and Hydroxy Butadiene Adducts[a]

	isoprene adducts				butadiene adducts		
	simulation time, ps	av temp, K	ΔE[b]		simulation time, ps	av temp, K	ΔE[b]
1a[c]	20	210.39 ± 34.57	0.412	1a[c]	25	182.78 ± 53.24	2.279
1b[c]	20	204.24 ± 34.73	0.824	1b[c]	25	233.71 ± 55.09	0.685
2a[c]	20	205.37 ± 52.20	0.534	$2_{II}{}^{a}$[c]	25	239.40 ± 100.60	0.372
2b[c]	20	197.98 ± 42.57	0.657	$2_{II}{}^{b}$[c]	25	243.37 ± 66.91	0.287
3a[c]	20	207.45 ± 36.39	0.478	$2_{III}{}^{a}$[c]	25	238.65 ± 72.84	0.579
3b[c]	20	199.56 ± 47.70	0.601	$2_{III}{}^{c}$	25	244.45 ± 88.96	0.134
4a[c]	20	199.15 ± 42.61	0.710				
4b[c]	20	171.44 ± 78.70	0.796				

[a]Initial temperature (computed from kinetic energy) for all of the isoprene adducts is 450.007 K, whereas that for the butadiene adducts is 572.736 K. [b]Energy conservation during dynamics in millihartrees. [c]Adduct number and simulation type.

2.1. Brief Overview of the Theoretical Basis for the Extended Lagrangian ab Initio Molecular Dynamics Method, Atom-Centered Density Matrix Propagation.

The method of AIMD relies on calculation of the electronic potential surface traversed by the nuclei on-the-fly during the dynamics procedure. Both Born−Oppenheimer molecular dynamics (BOMD),[35−42,53] as well as Car−Parrinello (CP) dynamics,[38,41,53−55] are part of this category. The CP scheme differs from the BO dynamics approach in that the wave functions are propagated together with the classical nuclear degrees of freedom using an extended Lagrangian.[56,57] This, in turn, relies on an adjustment of the relative nuclear and electronic time scales, which facilitates the adiabatic propagation of the electronic wave function in response to the nuclear motion with suitably large time steps. This adjustment of time scales through the use of a fictitious electronic wave function kinetic energy and inertia, enables the CP approach to predict effectively similar nuclear dynamics on the BO surface at reduced cost. In this respect, CP differs from methods which rigorously treat the detailed dynamics (rather than structure) of the electrons. (See ref 39 and references therein.) The CP method is essentially an extended Lagrangian[56,57] dynamics scheme in which the electronic degrees of freedom are not iterated to convergence at each step but are instead treated as fictitious dynamical variables and propagated along with the nuclear degrees of freedom by a simple adjustment of time scales. The resultant energy surface remains close to a converged adiabatic electronic surface. Numerous important examples of applications with density functional theory and the CP method are now well-documented in the literature (see, e.g., refs 41 and 54). In the original CP approach, the Kohn−Sham molecular orbitals, expanded in a plane-wave basis, were chosen as dynamical variables to represent the electronic degrees of freedom.[53] However, this is not the only possible choice. An alternative approach is to propagate the individual elements of the reduced one-particle density matrix, **P**.

In ADMP,[40,45−49,51] atom-centered Gaussian basis sets are employed to represent the single-particle electronic density matrix within an extended Lagrangian formalism. Here the basis functions follow the nuclei. The ADMP method has several attractive features. Systems can be simulated by accurately treating all electrons or by using pseudopotentials. Through the use of smaller values for the tensorial fictitious mass (to be discussed below), relatively large time steps can be employed and lighter atoms such as hydrogens are routinely used. A wide variety of exchange-correlation functionals can be utilized, including hybrid density functionals such as B3LYP. Atom-centered functions can be used with the appropriate physical boundary conditions for molecules, polymers, surfaces, and solids, without the need to treat replicated images to impose 3d periodicity. This is particularly relevant to atmospheric clusters that are described here. Hybrid quantum-mechanics/molecular mechanics (QM/MM) generalization has been demonstrated.[51] ADMP has been demonstrated through the treatment of several interesting problems including the following:[6,8,9,19,20,22,23,25,26,46,48,51] (a) a recent demonstration that dynamical effects are critical in obtaining good vibrational spectroscopic properties of flexible systems;[8,19−21,25,26] (b) the prediction of the "amphiphilic" nature of the hydrated proton,[20,22,58] which has now been confirmed by many experimental[59−61] and theoretical studies.[62−66]

The ADMP equations of motion for the nuclei and density matrix are derived from the extended Lagrangian:

$$\mathcal{L} = \frac{1}{2}\text{Tr}[\mathbf{V}^{\mathbf{T}}\mathbf{M}\mathbf{V}] + \frac{1}{2}\text{Tr}[(\underline{\mu}^{1/4}\mathbf{W}\underline{\mu}^{1/4})^2] - E(\mathbf{R_C}, \mathbf{P}, R_{\text{QM}}) - \text{Tr}[\Lambda(\mathbf{P}^2 - \mathbf{P})] \tag{4}$$

where **R**, **V**, and **M** are the nuclear positions, velocities, and masses and **P**, **W**, and $\underline{\mu}$ are the density matrix, the density matrix velocity, and the fictitious mass tensor for the electronic degrees of freedom. Λ is a Lagrangian multiplier matrix used to impose N-representability of the single-particle density matrix. The energy, $E(\mathbf{R,P})$, is calculated using McWeeny purification, $\tilde{\mathbf{P}} = 3\mathbf{P}^2 - 2\mathbf{P}^3$,

$$E = \text{Tr}\left[\mathbf{h}'\tilde{\mathbf{P}}' + \frac{1}{2}\mathbf{G}'(\tilde{\mathbf{P}}')\tilde{\mathbf{P}}'\right] + E_{\text{xc}} + V_{\text{NN}}$$

$$= \text{Tr}\left[\mathbf{h}\tilde{\mathbf{P}} + \frac{1}{2}\mathbf{G}(\tilde{\mathbf{P}})\tilde{\mathbf{P}}\right] + E_{\text{xc}} + V_{\text{NN}} \tag{5}$$

Here, $\mathbf{h}'$ is the one-electron matrix in the nonorthogonal Gaussian basis and $\mathbf{G}'(\tilde{\mathbf{P}}')$ is the two-electron matrix for Hartree−Fock calculations, but for density functional theory (DFT) it represents the Coulomb potential. The term E_{xc} is the energy obtained from a DFT exchange-correlation functional (for Hartree−Fock $E_{\text{xc}} = 0$), while V_{NN} represents the nuclear repulsion energy. In the orthonormal basis, these matrices are $\mathbf{h} = \mathbf{U}^{-\mathbf{T}}\mathbf{h}'\mathbf{U}^{-1}$, etc., where the overlap matrix for the nonorthogonal Gaussian basis, $\mathbf{S}'$, is factorized to yield $\mathbf{S}' = \mathbf{U}^{\mathbf{T}}\mathbf{U}$. There are a number of choices for the transformation matrix **U**, e.g., **U** can be obtained from Cholesky decomposition[67] of $\mathbf{S}'$ or $\mathbf{U} = \mathbf{S}'^{1/2}$ for Löwdin symmetric orthogonalization. The matrix **U** can also include an additional transformation so that overall rotation of the system is factored out of the propagation of the density. The density matrix in the orthonormal basis, **P**, is related to the density matrix in the nonorthogonal Gaussian basis, $\mathbf{P}'$, by $\mathbf{P} \equiv \mathbf{UP}'\mathbf{U}^{\mathbf{T}}$.

With regard to the extended Lagrangian in eq 4, also see ref 68, where this Lagrangian has been generalized to include multiple diabatic states and their influence on quantum nuclear dynamics.

The equations of motion for the above formalism are

$$\mathbf{M}\frac{d^2\mathbf{R}}{dt^2} = -\left.\frac{\partial E(\mathbf{R}, \mathbf{P})}{\partial \mathbf{R}}\right|_{\mathbf{P}} \tag{6}$$

$$\underline{\mu}^{1/2}\frac{d^2\mathbf{P}}{dt^2}\underline{\mu}^{1/2} = -\left[\left.\frac{\partial E(\mathbf{R}, \mathbf{P})}{\partial \mathbf{P}}\right|_{\mathbf{R}} + \Lambda\mathbf{P} + \mathbf{P}\Lambda - \Lambda\right] \tag{7}$$

These equations are numerically integrated using the velocity Verlet scheme.[45,69] The updated nuclear positions and density matrix elements are computed using

$$\mathbf{R}_{(t+\Delta t)} = \mathbf{R}_{(t)} + \mathbf{V}_{(t)}\Delta t$$
$$- \frac{\Delta t^2}{2}\mathbf{M}^{-1}\left[\left.\frac{\partial E(\mathbf{R}_{(t)}, \mathbf{P}_{(t)})}{\partial\mathbf{R}_{(t)}}\right|_{\mathbf{P}_{(t)}}\right] \tag{8}$$

$$\mathbf{P}_{(t+\Delta t)} = \mathbf{P}_{(t)} + \mathbf{W}_{(t)}\Delta t - \frac{\Delta t^2}{2}\underline{\mu}^{-1/2}\left[\left.\frac{\partial E(\mathbf{R}_{(t)}, \mathbf{P}_{(t)})}{\partial\mathbf{P}_{(t)}}\right|_{\mathbf{R}_{(t)}}\right.$$
$$\left. + \Lambda_{(t)}\mathbf{P}_{(t)} + \mathbf{P}_{(t)}\Lambda_{(t)} - \Lambda_{(t)}\right]\underline{\mu}^{-1/2} \tag{9}$$

while the updated nuclear velocities and density matrix velocities are determined using

$$\mathbf{V}_{(t+\Delta t)} = \mathbf{V}_{(t)} - \frac{\Delta t}{2}\mathbf{M}^{-1}\left[\left(\left.\frac{\partial E(\mathbf{R}_{(t+\Delta t)}, \mathbf{P}_{(t+\Delta t)})}{\partial\mathbf{R}_{(t+\Delta t)}}\right|_{\mathbf{P}_{(t+\Delta t)}}\right)\right.$$
$$\left. + \left(\left.\frac{\partial E(\mathbf{R}_{(t)}, \mathbf{P}_{(t)})}{\partial\mathbf{R}_{(t)}}\right|_{\mathbf{P}_{(t)}}\right)\right] \tag{10}$$

$$\mathbf{W}_{(t+\Delta t)} = \mathbf{W}_{(t)} - \frac{\Delta t}{2}\underline{\mu}^{-1/2}$$
$$\times\left[\left[\left(\left.\frac{\partial E(\mathbf{R}_{(t+\Delta t)}, \mathbf{P}_{(t+\Delta t)})}{\partial\mathbf{P}_{(t+\Delta t)}}\right|_{\mathbf{R}_{(t+\Delta t)}}\right)\right.\right.$$
$$+ \Lambda_{(t+\Delta t)}\mathbf{P}_{(t+\Delta t)} + \mathbf{P}_{(t+\Delta t)}\Lambda_{(t+\Delta t)}$$
$$\left. - \Lambda_{(t+\Delta t)}\right) + \left(\left.\frac{\partial E(\mathbf{R}_{(t)}, \mathbf{P}_{(t)})}{\partial\mathbf{P}_{(t)}}\right|_{\mathbf{R}_{(t)}}\right.$$
$$\left.\left. + \Lambda_{(t)}\mathbf{P}_{(t)} + \mathbf{P}_{(t)}\Lambda_{(t)} - \Lambda_{(t)}\right)\right]\underline{\mu}^{-1/2} \tag{11}$$

The gradient terms involved in the equations of motion are

$$\left.\frac{\partial E(\mathbf{R}, \mathbf{P})}{\partial\mathbf{P}}\right|_{\mathbf{R}} = 3\mathbf{FP} + 3\mathbf{PF} - 2\mathbf{FP}^2 - 2\mathbf{PFP} - 2\mathbf{P}^2\mathbf{F} \tag{12}$$

where $\mathbf{F}$ is the Fock matrix and in the nonorthogonal basis

$$\mathbf{F}'_{\nu,\sigma} \equiv \mathbf{h}'_{\nu,\sigma} + \mathbf{G}'(\tilde{\mathbf{P}}')_{\nu,\sigma} + \frac{\partial E_{xc}}{\partial\mathbf{P}'} \tag{13}$$

while the orthogonal basis Fock matrix is $\mathbf{F} = \mathbf{U}^{-T}\mathbf{F}'\mathbf{U}^{-1}$. The nuclear gradients are

$$\left.\frac{\partial E}{\partial\mathbf{R}}\right|_{\mathbf{P}} = \left\{\text{Tr}\left[\frac{d h'}{d\mathbf{R}}\tilde{\mathbf{P}}' + \frac{1}{2}\left.\frac{\partial\mathbf{G}'(\mathbf{P}')}{\partial\mathbf{R}}\right|_{\mathbf{P}'}\tilde{\mathbf{P}}'\right]\right.$$
$$- \text{Tr}\left[\mathbf{F}'\tilde{\mathbf{P}}'\frac{d\mathbf{S}'}{d\mathbf{R}}\tilde{\mathbf{P}}'\right] + \left.\frac{\partial E_{xc}}{\partial\mathbf{R}}\right|_{\mathbf{P}} + \left.\frac{\partial V_{NN}}{\partial\mathbf{R}}\right\}$$
$$+ \text{Tr}\left[[\tilde{\mathbf{P}}, \mathbf{F}]\left(\tilde{\mathbf{Q}}\frac{d\mathbf{U}}{d\mathbf{R}}\mathbf{U}^{-1} - \tilde{\mathbf{P}}\mathbf{U}^{-T}\frac{d\mathbf{U}^T}{d\mathbf{R}}\right)\right] \tag{14}$$

where $\tilde{\mathbf{Q}} \equiv \mathbf{I} - \tilde{\mathbf{P}}$. It has been shown that[45,47] as the commutator $[\tilde{\mathbf{P}}, \mathbf{F}] \to 0$, the nuclear forces tend to those used in the standard Born–Oppenheimer MD.[70] However, in ADMP, the magnitude of the commutator $[\tilde{\mathbf{P}}, \mathbf{F}]$ is nonnegligible and hence the general expression for the nuclear gradients[40,47] in eq 14 is used.

The conjugate Hamiltonian derived from a Legendre transform[71] of the Lagrangian in eq 4 is

$$\mathcal{H}(\mathbf{P}, \mathcal{W}, \mathbf{R}, \mathcal{V}, t)$$
$$= \text{Tr}(\mathcal{W}\mathbf{W}) + \text{Tr}(\mathcal{V}^T\mathbf{V}) - \mathcal{L}(\mathbf{P}, \mathbf{W}, \mathbf{R}, \mathbf{V}, t) \tag{15}$$

where $\mathcal{W}$ and $\mathcal{V}$ are the conjugate momenta for $\mathbf{P}$ and $\mathbf{R}$, respectively, and are given by

$$\mathcal{W} = \frac{\partial\mathcal{L}}{\partial\mathbf{W}} = \underline{\mu}^{1/2}\mathbf{W}\underline{\mu}^{1/2} \tag{16}$$

$$\mathcal{V} = \frac{\partial\mathcal{L}}{\partial\mathbf{V}} = \mathbf{MV} \tag{17}$$

The Hamiltonian in eq 15 is conservative; i.e., $d\mathcal{H}/dt = 0$. Hence the integrated velocity Verlet equations obtained from eqs 6 and 7 conserve the total energy to within the microhartree range for time steps of the order of 0.25 fs. Since the velocity Verlet equations are obtained from a third-order[49] Trotter factorization[72,73] of the Liouville equation for eqs 6 and 7,[49] the integration error grows as the third power of the chosen dynamics time step. Hence, angular momentum is also well-conserved within the numerical limits enforced by the third-order integration scheme. It must however be emphasized that this simulation scheme is purely classical from the point of view of the nuclei. One of the deficiencies of such an approach is the restricted zero-point constraint.[74−76] The problem of constraining classical dynamics equations through the influence of the zero-point vibrational modes which in turn include the full anharmonic potential surface is a challenging and unsolved problem in chemical physics. Common approaches[74−76] include constraining the dynamics using modes obtained through a local harmonic approximation. Our approach here does not include these effects.

Similar to CP, ADMP represents fictitious dynamics where the density matrix is propagated instead of being converged.
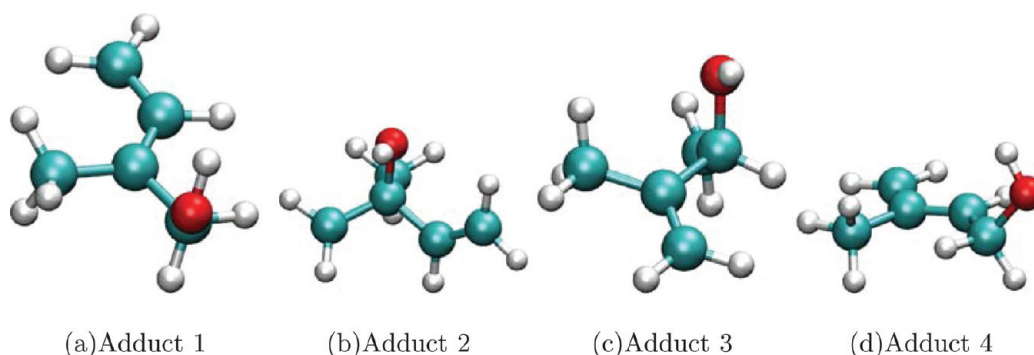
D

dx.doi.org/10.1021/jp212330e | J. Phys. Chem. A XXXX, XXX, XXX−XXX

Figure 1. Optimized starting structures for the four hydroxy−isoprene adducts. Level of theory: B3LYP/6-311++G(D,P).

The accuracy and efficiency is governed by the choice of the fictitious mass tensor, $\underline{\mu}$; hence one must be aware of the limits on this quantity. We have derived two independent criteria[45,47] that place bounds on the choice of the fictitious mass. First, the choice of the fictitious mass determines the magnitude of the commutator $[\tilde{\mathbf{P}}, \mathbf{F}]$, thus determining the extent of deviation from the Born−Oppenheimer surface:[47]

$$\|[\mathbf{F}, \mathbf{P}_{approx}]\|_F \geq \frac{1}{\|[\mathbf{P}_{approx}, \mathbf{W}]\|_F} \times \left| \mathrm{Tr}\left[\mathbf{W}\underline{\mu}^{1/2}\frac{d\mathbf{W}}{dt}\underline{\mu}^{1/2} \right] \right| \quad (18)$$

where $\|[...]\|_F$ is the Frobenius norm[67,77] of the commutator and is defined as $\|[A]\|_F = \left(\sum_{i,j} (A_{i,j})^2 \right)^{1/2}$. Second, the rate of change of the fictitious kinetic energy,

$$\frac{d\mathcal{H}_{fict}}{dt} = \mathrm{Tr}\left[\mathbf{W}\underline{\mu}^{1/2}\frac{d^2\mathbf{P}}{dt^2}\underline{\mu}^{1/2} \right]$$

$$= -\mathrm{Tr}\left[\mathbf{W}\left(\frac{\partial E(\mathbf{R}, \mathbf{P})}{\partial \mathbf{P}}\bigg|_{\mathbf{R}} + \mathbf{\Lambda P} + \mathbf{P\Lambda} - \mathbf{\Lambda} \right) \right] \quad (19)$$

is to be bounded and oscillatory, and this again is determined by the choice of fictitious mass tensor. We have shown that ADMP gives results that are in good agreement with BOMD and is computationally superior to BOMD.[46] However, one must monitor the quantities in eqs 18 and 19 to ascertain that the ADMP dynamics is physically consistent. In all applications studied to date,[8,19,20,22,40,45,46,51] these conditions are satisfied, thus yielding a computationally efficient and accurate approach to model dynamics on the Born−Oppenheimer surface.

Current implementation of the ADMP approach has been found to be computationally superior to Born−Oppenheimer dynamics.[46] This important result can be conceptualized on the basis of the following: In Born−Oppenheimer dynamics, the density matrix is to be converged at every dynamics step. Assuming that the largest possible time step is used during dynamics, self-consistent field (SCF) convergence requires approximately 8−12 SCF steps. (This depends on the convergence threshold, and difficult cases such as transition metal complexes may require more SCF steps.) In ADMP, on
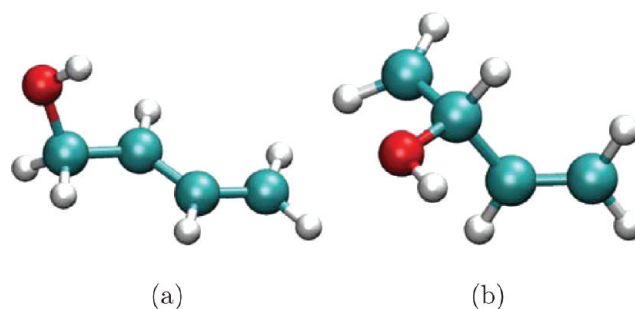

Figure 2. Optimized starting structures for the two hydroxy−butadiene adducts. Level of theory: B3LYP/6-311++G(D,P).

the contrary, only the equivalent of 1 SCF step is required per dynamics step; this 1 SCF step is necessary to calculate the Fock matrix required for propagating the density matrix. (A brief review of ADMP is presented in section 2.1.) Both BOMD and ADMP evaluate the gradient of energy with respect to nuclear coordinates, and this calculation requires approximately the same amount of time in both methods. Note that the gradients used in ADMP are more general than those used in BOMD[40,47] on account of the nonnegligible magnitude of the commutator of the Fock and density matrix. (See section 2.1 and ref 47 for details.) However, the additional terms require no significant computation over the standard BOMD gradient calculation. The calculation of nuclear force requires approximately 3 times as much computation time as a single SCF cycle. This makes ADMP faster than BOMD by over a factor of 4 per dynamics step. However, the requirement that the ADMP energies oscillate about the BO values with small amplitudes[45] implies that ADMP step sizes cannot be as large at those in BO dynamics. But good energy conservation, which applies to both methods, limits the BO steps to at most twice those of ADMP.[46] (ADMP already uses reasonably large time steps on account of smaller values for the fictitious mass and an innovative tensorial fictitious mass scheme.[45]) This allows ADMP to be over a factor of 2 superior to BOMD, but this estimate is only for cases where the SCF convergence in BOMD is not difficult.[46] The hard to converge cases would require more SCF steps (or a better SCF convergence algorithm), thus making ADMP more efficient as compared to BOMD for these cases. Furthermore, computational improvements that speed up the gradient evaluation will tilt this comparison further toward ADMP.

2.2. Vibrational Energy Density and Energy Redistribution from AIMD Simulations. The dynamically averaged vibrational density of states were computed by using
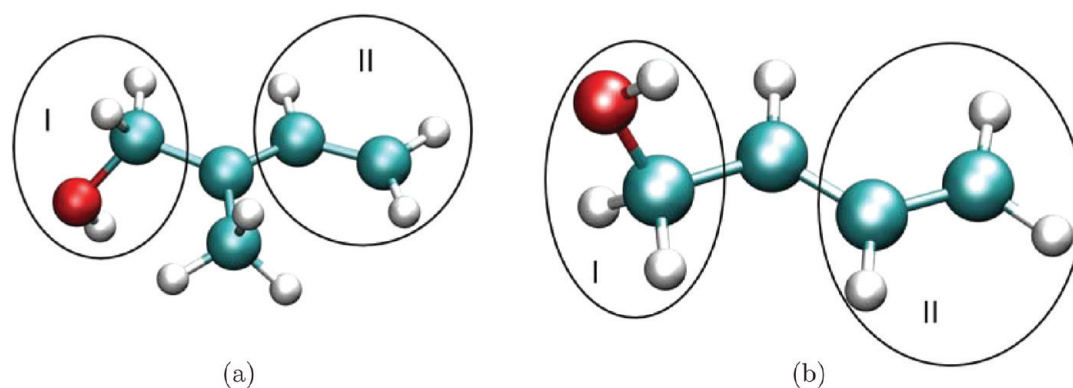
Figure 3. Structure of (a) hydroxy−isoprene, adduct 1, and (b) hydroxy−butadiene, adduct 1, showing the fragments used for AIMD simulations. In each case fragment III includes the central carbon.

Table 2. Initial Kinetic Energy Distribution (eV) for the Isoprene−OH Adduct Simulations[a]

	adduct 1		adduct 2		adduct 3		adduct 4	
fragment	1a	1b	2a	2b	3a	3b	4a	4b
I	0.556	0.209	0.596	0.191	0.430	0.197	0.483	0.209
II	0.210	0.560	0.172	0.577	0.219	0.554	0.290	0.557
III	0.048	0.045	0.046	0.047	0.166	0.064	0.042	0.048

[a]The precise vibrational modes that are excited to yield this unsymmetric energy distribution are noted in discussed in Tables 4−7. The Appendix provides a short discussion to this effect.

the Fourier transform of the nuclear velocity autocorrelation function (FT-VAC):

$$I_V(\omega) = \lim_{T \to \infty} \int_{t=0}^{t=T} dt \, \exp(-i\omega t) \langle \mathbf{V}(0) \cdot \mathbf{V}(t) \rangle$$

$$= \lim_{T \to \infty} \sum_{i=1}^{N_{atoms}} \sum_{j=1}^{3} \int_{t=0}^{t=T} dt \, \exp(-i\omega t)$$

$$\times \int_{t'=0}^{t'=T} dt' V_{i,j}(t') \, V_{i,j}(t'+t)$$

$$= \lim_{T \to \infty} \sum_{i=1}^{N_{atoms}} \sum_{j=1}^{3} \left| \int_{t=0}^{t=T} dt \, \exp(-i\omega t) \, V_{i,j}(t) \right|^2 \tag{20}$$

where the term $\langle ... \rangle$, in the first equation, indicates ensemble average and is equal to the t'-integral in the second equation under the ergodicity condition. The quantity $V_{i,j}(t)$ is the velocity along the jth component for the ith atom. We have used the convolution theorem[78] to reduce the second equation to the third equation. In ref 9 we also construct the quantum-mechanical analogue of eq 20, using the flux operator, and demostrate that vibrational states are obtained from such a formalism with intensities proportional to kinetic energy. Also see refs 6, 8, and 19−27

Energy redistribution in chemical systems has been well-studied[79−91] in the past few decades. Influenced by the early work of Fermi et al.,[79,87] one of us formulated a scheme in refs 25 and 26 to decompose and assign the finite temperature vibrational density of states utilizing harmonic normal mode vectors that are obtained by diagonalizing the nuclear Hessian matrix at a minimum energy configuration. Specifically, since mass-weighted normal mode vectors are eigenstates of the Hessian matrix and hence form a complete orthonormal set, we

can expand $\mathcal{V}^T(\omega)$, the finite time (T) Fourier transform of mass-weighted velocities, $\{\mathcal{V}(t) : \mathcal{V}_{i,j}(t) \equiv \sqrt{M_i} V_{i,j}(t)\}$:

$$\tilde{\mathcal{V}}_{j,k}^T(\omega) = \int_0^T dt \, \exp[-i\omega t] \, \mathcal{V}_{j,k}(t) \tag{21}$$

in such a basis as

$$\overrightarrow{\tilde{\mathcal{V}}}^T(\omega) = \sum_i C_{i,T}(\omega) \vec{H}_i \tag{22}$$

where $\vec{H}_i$ is the ith Harmonic (mass-weighted) normal mode vector. In ref 9, the scheme above has been generalized to resolve transient, time-dependent spectral properties through introduction of a windowed Fourier transform or short-time Fourier transform:[92−95]

$$\tilde{\mathcal{V}}_{j,k}^{t',T}(\omega, t) = \int_0^T dt'' \, \exp[-i\omega t''] \, \theta(t''; t, t') \, \mathcal{V}_{j,k}(t'') \tag{23}$$

and the associated velocity autocorrelation function in the time window, $[t,t']$, as constrained by the window function $\theta(t''; t, t')$ is

$$I_V(\omega; t', t) = \sum_{i=1}^{N_{atoms}} \sum_{j=1}^{3} \frac{1}{M_i} |\tilde{\mathcal{V}}_{i,j}^{t',T}(\omega, t)|^2 \tag{24}$$

Notice that as $\theta(t''; t, t')$ tends to identity in the time window $[0, T]$, $I_V(\omega; t, t) \to I_V(\omega)$. Transient behavior has been shown to arise in ref 9 through the appropriate choice of $\theta(t''; t, t')$. In the studies presented here, $\theta(t''; t, t')$ has been chosen to be a step function that is equal to one inside the window $[t, t']$ and zero otherwise. More precisely here, the functional form of $\theta(t''; t, t')$ is chosen such that there is no explicit dependence on t', but, instead, $\theta(t''; t, t') \equiv \theta(t''; t, |t-t'|)$. Thus, when $(t' - t)$ is chosen to be a constant, $I_V(\omega; t', t)$ is a function of ω and t. This provides a two-dimensional correlation spectrum, the evolution of which along the time axis provides temporal behavior.

In this paper we probe the energy redistribution phenomena using this expression. In a fashion complementary to eq 24, the $C_{i,T}(\omega)$ coefficients in eq 22 have been generalized in ref 9 using the time-dependent expression in eq 23 as

$$\overrightarrow{\widetilde{\mathcal{V}}}^{t',T}(\omega, t) = \sum_i C^{t'}_{i,T}(\omega, t)\vec{H}_i \tag{25}$$

Physical intepretations for eq 24 are discussed in section 2.2.1.

The expansion coefficients, $C_{i,T}(\omega)$ in eq 22, are the contribution of the ith normal mode vector to the Fourier transform of the velocity in eq 23, at frequency ω for a dynamics simulation of time-fragment length, T. The net contribution of the ith normal mode to the vibrational density of states in the frequency range $\Delta\omega \equiv [\omega_1, \omega_2]$, may then be

written as a superposition of all its contributions inside the frequency range:

$$C^{\Delta\omega}_{i,T} = \left[\int_{\omega_1}^{\omega_2} d\omega\, |C_{i,T}(\omega)|^2\right]^{1/2}$$
$$= \left[\int_{\omega_1}^{\omega_2} d\omega\, |\vec{H}_i \cdot \overrightarrow{\widetilde{\mathcal{V}}}^T(\omega)|^2\right]^{1/2} \tag{26}$$

It must be noted here that the contribution of mode i described in eq 26 is from the velocity spectrum and does not contain information about dipole (or IR) intensities. While all nuclear motions contribute to the FT-VAC, the dipole spectrum only contains those spectral features of the velocity spectrum that also have substantial dipole fluctuations (as in the experimental situation). To obtain the contribution from mode i to the dipole (or IR) spectrum, we utilize the harmonic IR intensities, I_i, as

$$D^{\Delta\omega}_{i,T} = I_i^{1/2} C^{\Delta\omega}_{i,T} \tag{27}$$

The quantity $|D^{\Delta\omega}_{i,t'}|^2$ may be interpreted as being proportional to the "corrected IR intensity", at a given temperature.
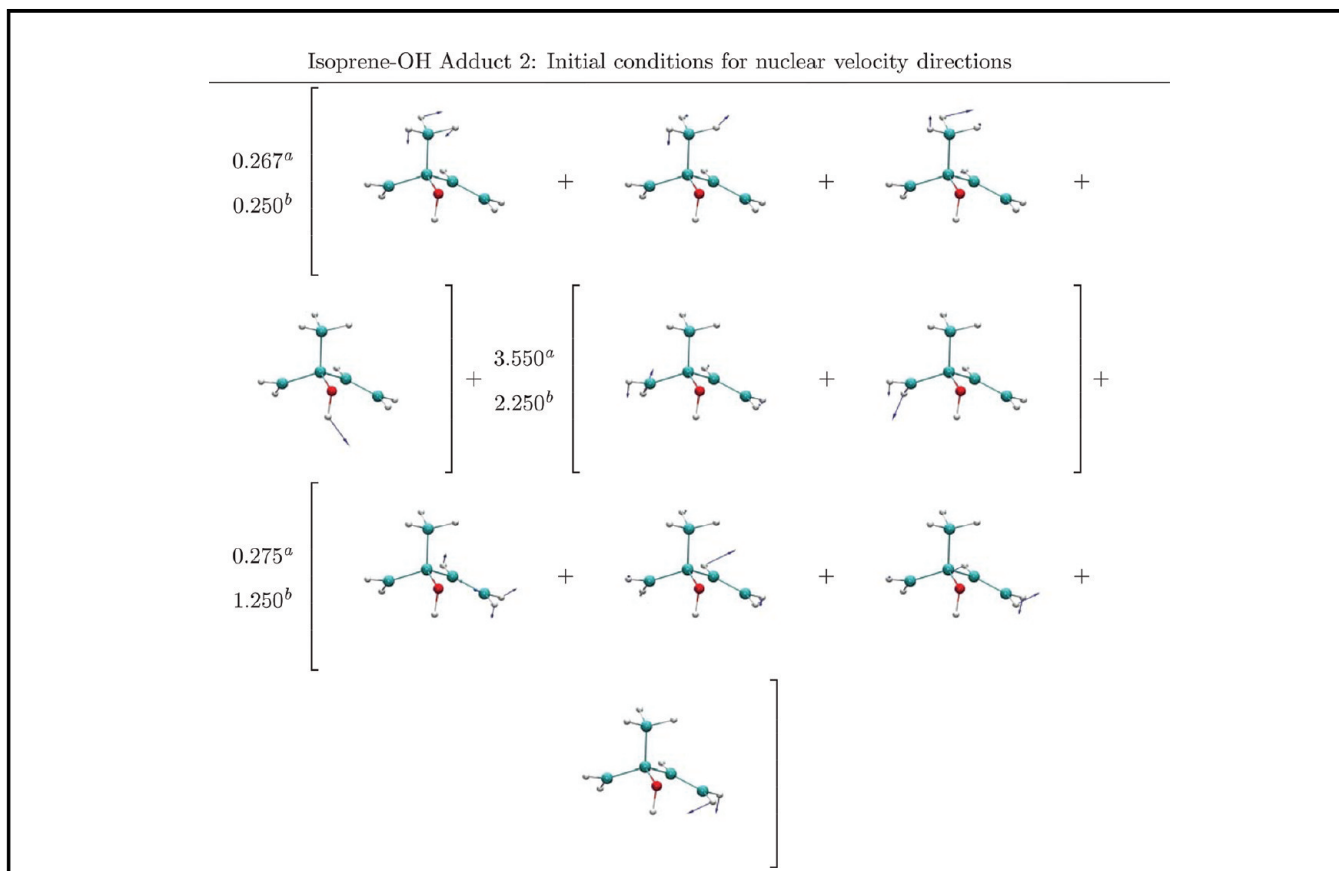
2.2.1. Physical Interpretation of Equation 24. It has been shown[9] that in the limit as $T \to \infty$ (in eq 23), using Parsevaal's theorem,[78] $\widetilde{\mathcal{V}}^{t',T}_{j,k}(\omega)$ may be interpreted as being proportional to the kinetic energy in the system at frequency ω for a time series of length T. [Note that the total kinetic energy at time t is $[1/2\sum_{j,k}(\mathcal{V}_{j,k}(t))^2]$.] The limit as $T \to \infty$ is a rather subtle

Table 3. Initial Kinetic Energy Distribution (eV) for the Butadiene−OH Adduct Simulations[a]

	adduct 1		adduct 2$_{\text{II}}$		adduct 2$_{\text{III}}$	
fragment	1a	1b	2a	2b	3a	3b
I	0.565	0.193	0.572	0.227	0.576	0.209
II	0.202	0.576	0.195	0.541	0.192	0.557
III	0.047	0.046	0.048	0.047	0.046	0.048

[a]The precise vibrational modes that are excited to yield this unsymmetric energy distribution are noted in discussed in Tables 8−10. The Appendix provides a short discussion to this effect.

Table 4. Pumped Vibrational Modes for Isoprene−OH Adduct 1 (Vibrational Modes Represented with Arrows Proportional to the Harmonic Displacement Vectors)

Isoprene-OH Adduct 1: Initial conditions for nuclear velocity directions
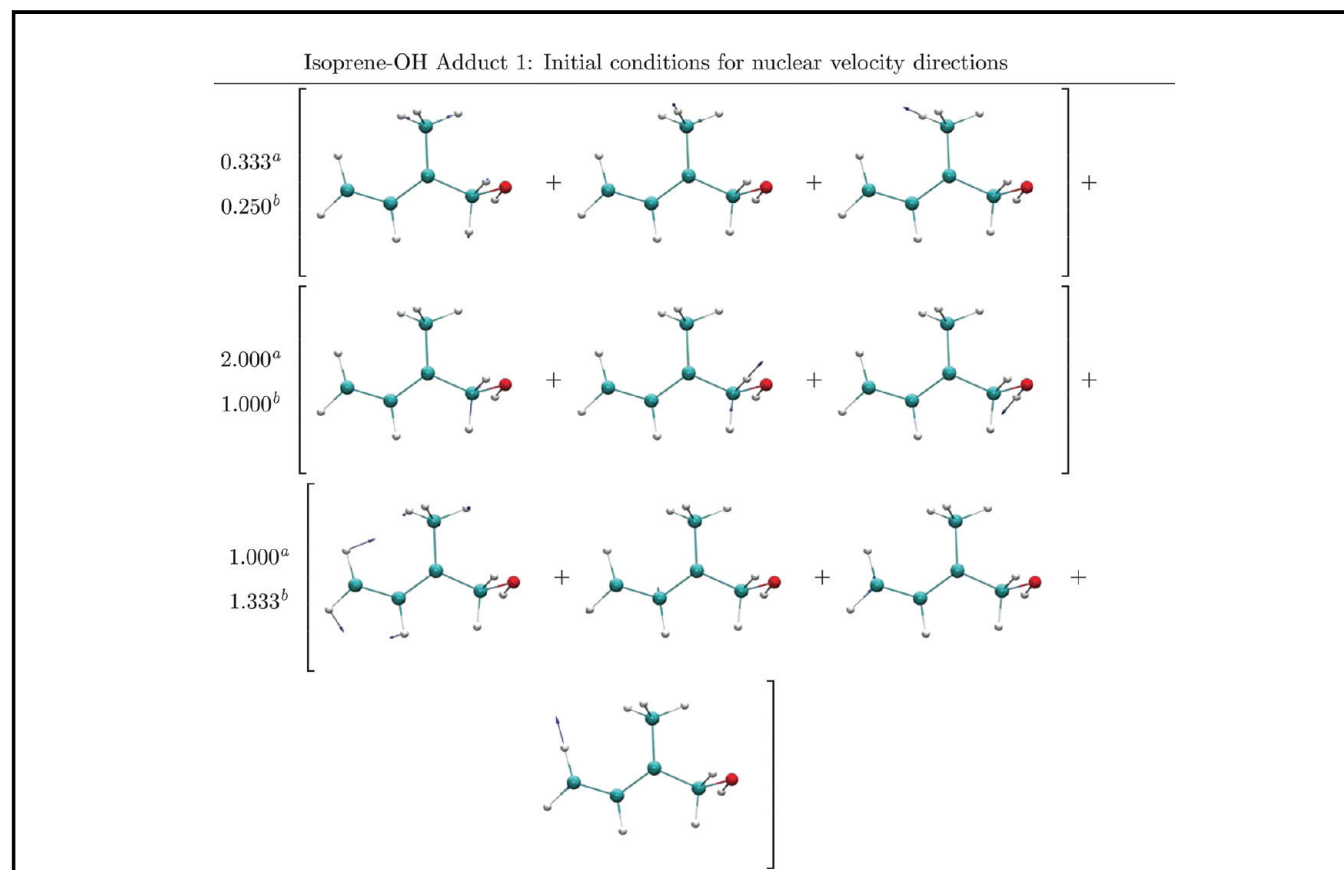
[a]Simulation 1a. [b]Simulation 1b.

Table 5. Pumped Vibrational Modes for Isoprene−OH Adduct 2 (Vibrational Modes Represented with Arrows Proportional to the Harmonic Displacement vectors)

Isoprene-OH Adduct 2: Initial conditions for nuclear velocity directions

[a]Simulation 2a. [b]Simulation 2b.

argument here and is to be interpreted as requiring T to be *large enough* such that all molecular motions appearing in $\mathcal{V}(t)$ are well-sampled in the time fragment of length T. To inspect the physical interpretation of $I_V(\omega;t',t)$, we note that

$$
\frac{1}{T}\int d\omega I_V(\omega;\, t',\, t) = \sum_{i=1}^{N_{atoms}}\sum_{j=1}^{3}\frac{1}{TM_i}
$$
$$
\times \int d\omega\, |\tilde{\mathcal{V}}_{i,j}^{t',T}(\omega,t)|^2
$$
$$
= \sum_{i=1}^{N_{atoms}}\sum_{j=1}^{3}\frac{1}{TM_i}\int dt''
$$
$$
\times |\theta(t'';\,t,\,t')\,\mathcal{V}_{i,j}(t)|^2 \tag{28}
$$

where we used Parsevaal's theorem[78] between the second and third expressions. Furthermore,

$$
\frac{1}{T}\int d\omega I_V(\omega;\, t',\, t) = \sum_{i=1}^{N_{atoms}}\frac{1}{TM_i}\int dt''
$$
$$
\times |\theta(t'';\,t,\,t')|^2\Big[\sum_{j=1}^{3}|\mathcal{V}_{i,j}(t)|^2\Big]
$$
$$
= \sum_{i=1}^{N_{atoms}}\frac{1}{TM_i}\langle\mathcal{V}_i\cdot\mathcal{V}_i\rangle_\theta \tag{29}
$$

where $\langle...\rangle_\theta$ represents a constrained ensemble average, under conditions of ergodicity. Here θ represents the constraint weight. For the case where $\theta(t'';t,t')$ is a step function equal to one inside the time window $[t,\,t']$ and zero otherwise,

$$
\frac{1}{T}\int d\omega I_V(\omega;\, t',\, t) = \sum_{i=1}^{N_{atoms}}\frac{1}{TM_i}\int_{t}^{t'}dt''
$$
$$
\times \Big[\sum_{j=1}^{3}|\mathcal{V}_{i,j}(t)|^2\Big]
$$
$$
= \sum_{i=1}^{N_{atoms}}\frac{1}{TM_i}\langle\mathcal{V}_i\cdot\mathcal{V}_i\rangle_{[t,t']} \tag{30}
$$

or

$$
\frac{1}{T}\int d\omega I_V(\omega;\, t',\, t) = 2\sum_{i=1}^{N_{atoms}}\langle\mathcal{K}_i\rangle_{[t,t']} = 2\langle\mathcal{K}\rangle_{[t,t']} \tag{31}
$$

The quantity $\mathcal{K}$ represents the total kinetic energy. Thus, the quantity $I_V(\omega;t',t)$ is proportional to a kinetic energy density at frequency ω or energy, $\hbar\omega$, in the time window $[t,\,t']$, as enforced by the ensemble constraint θ. Furthermore, using the Virial theorem,[71,96] (where for a potential with polynomial dependence $V(x)=\alpha x^n$, the expectation values for potential and kinetic energies are related by $\langle\mathcal{K}\rangle = n\langle\mathcal{V}\rangle$), the right side

Table 6. Pumped Vibrational Modes for Isoprene–OH Adduct 3 (Vibrational Modes Represented with Arrows Proportional to the Harmonic Displacement Vectors)
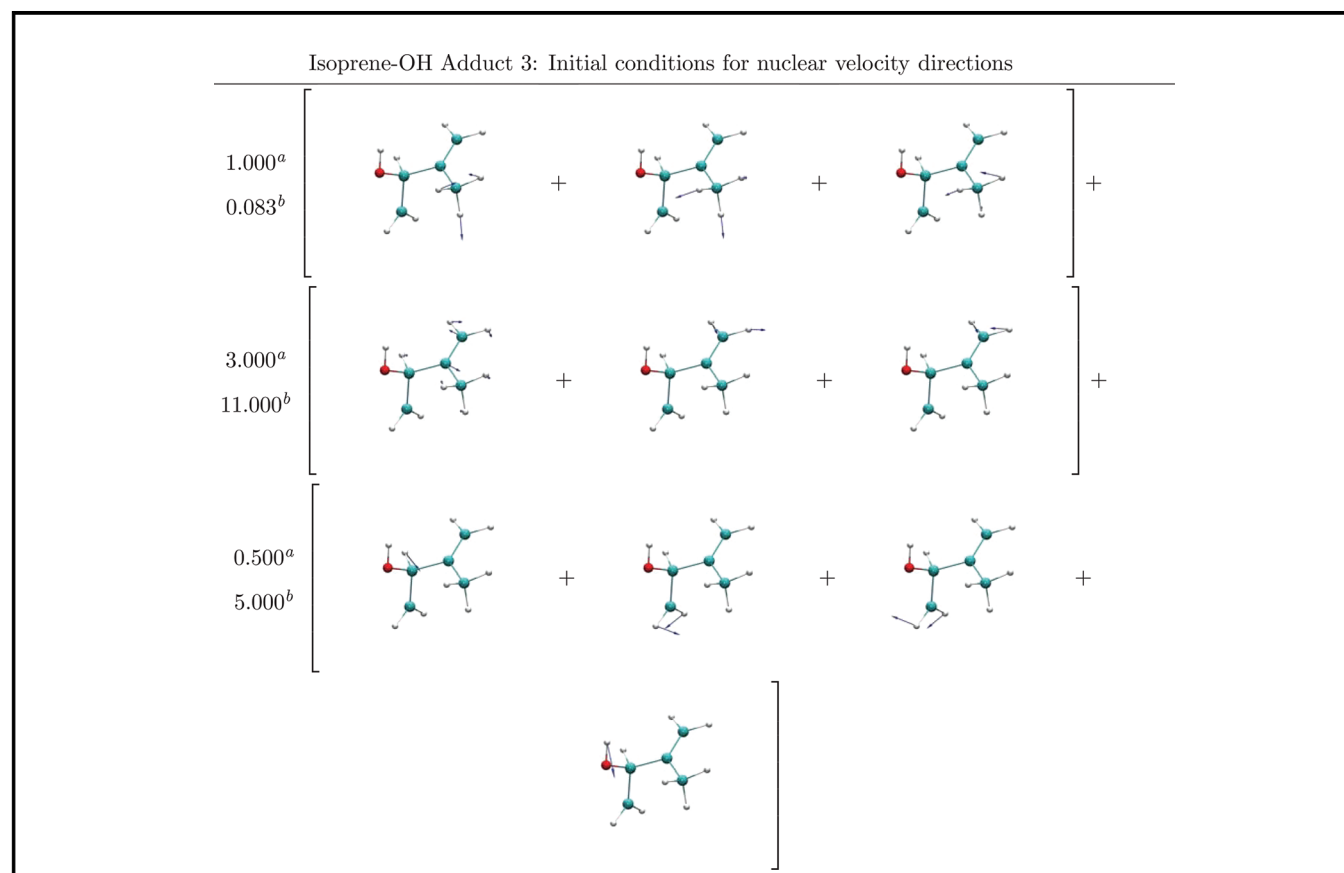
^{a}Simulation 3a. ^{b}Simulation 3b.

of eq 31 is also proportional to the average potential energy of the system under the ensemble constraint enforced by θ. Thus, $I_V(\omega;t',t)$ is also proportional to a potential energy density at frequency ω or energy, $\hbar\omega$. When $I_V(\omega;t',t)$ is normalized, it represents a density of kinetic energy (or potential energy) at frequency ω in the time window $[t, t']$. In the event that $\theta(t'';t,t')$ tends to identity in the time window $[0, T]$, $I_V(\omega; t',t) \rightarrow I_V(\omega)$ and the right side of eq 31 becomes an unconstrained ensemble average.
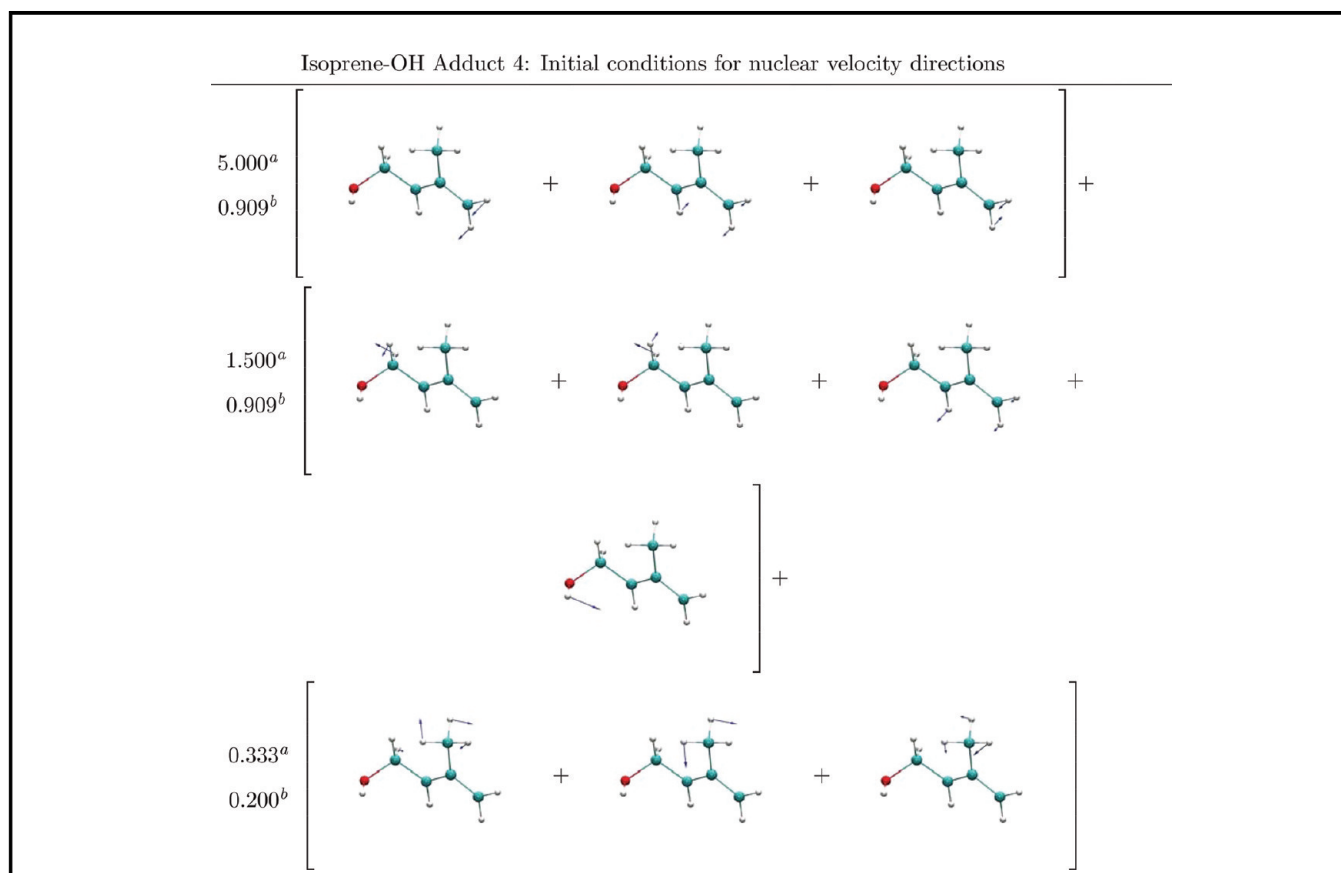
3. STRUCTURAL, VIBRATIONAL, AND DYNAMICAL PROPERTIES OF UNSOLVATED ISOPRENE–OH AND BUTADIENE–OH ADDUCTS

3.1. Initial Geometries for Simulations. The systems under study are the adducts resulting from the OH addition to alkenes. Two different volatile organics are considered: isoprene and 1,3-butadiene. 1,3-Butadiene is a hazardous, carcinogenic, and genotoxic air pollutant that is extensively used in industry,[97] while isoprene is the dominant natural VOC emitted by deciduous trees. Among atmospheric hydrocarbons, isoprene is a dominant molecule emitted by vegetation.[98] In fact, excluding methane, isoprene accounts for 40% of the hydrocarbon mass in the atmosphere.[99] Subsequently, this molecule has a significant role in atmospheric chemistry.

There are four possible hydroxyl adducts for isoprene and two for 1,3-butadiene. Equilibrium structures for all adducts were obtained from geometry optimizations using the Gaussian series of electronic structure programs[50] and are presented in
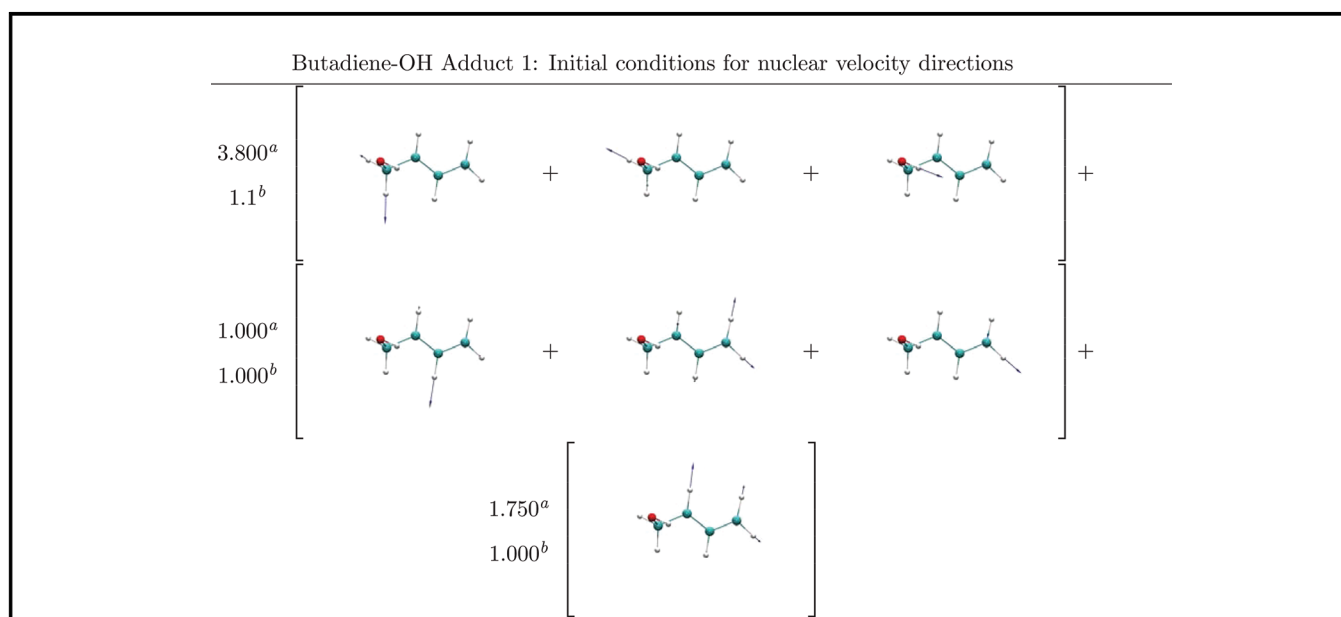
Figures 1 and 2. For the isoprene adducts, we first carried out relaxed scans about all of the four diherdral angles involving the C–C bonds in an effort to obtain the global minimum structure, rather than a local minima. For each rotational conformer, single-point energy calculations were carried out using the B3LYP/6-31G(D,P) level of theory. From the hundreds of conformers scanned for each adduct, the five *distinct* conformers with the lowest energy were subject to full optimization to obtain the equilibrium structure with the lowest energy followed by a frequency analysis at the B3LYP level of theory and 6-31G(D,P) and 6-311++G(D,P) basis sets. Common to all four equilibrium structures of the isoprene adducts, the O–H bond is always staggered with respect to the C–H bond of the same C atom. This is intuitive from basic organic chemistry where the staggered conformation is more stable than the eclipsed conformation. However, we also note that, in isoprene adduct 1, there is a five-membered O–C–C–C(Me)–H ring present. We have calculated the angle between the H–O–H(Me) atoms to be 102.85°, indicating that the lone pair on the oxygen atom is directed toward methyl proton, thereby forming a CH-hydrogen bond-like moeity as part of the five-membered ring. No such five-membered ring formation is present in adducts 2 and 3. In adduct 4, a six-membered ring with H–O–H(Me) angle of 112.88° is obtained; however, this conformation is not the lowest energy conformer, being 0.38 kcal/mol higher in energy than the lowest energy conformer shown pictorially in Figure 1d.
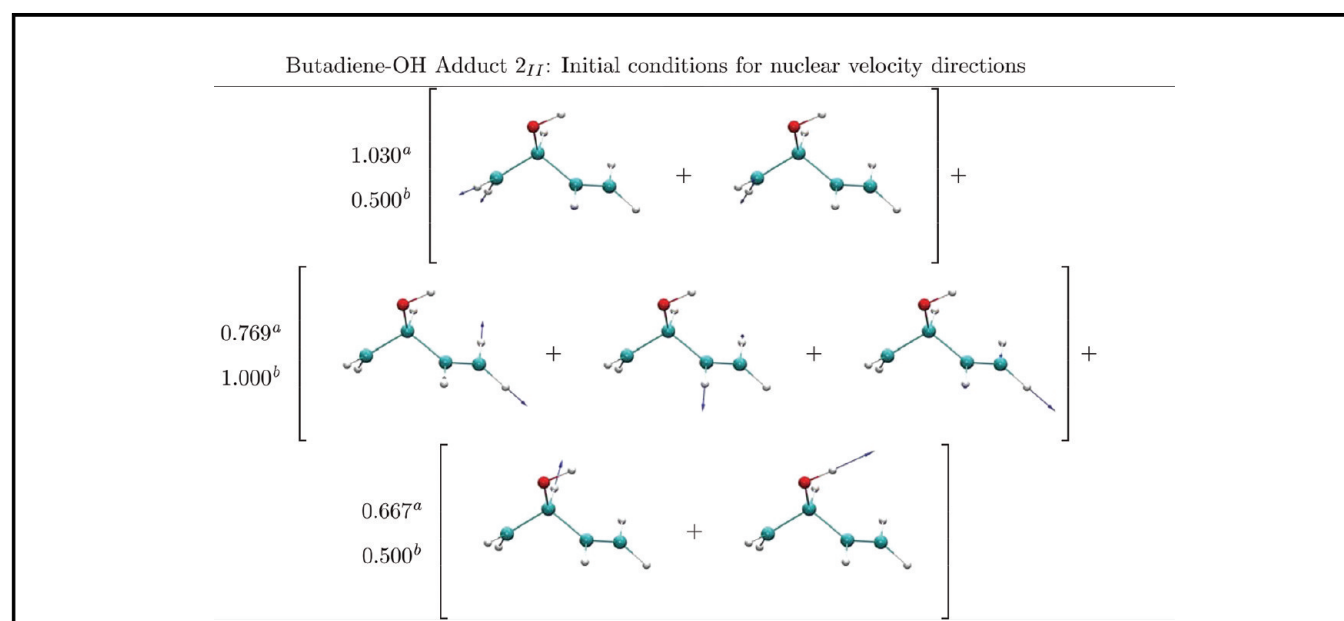
Table 7. Pumped Vibrational Modes for Isoprene–OH Adduct 4 (Vibrational Modes Represented with Arrows Proportional to the Harmonic Displacement Vectors)

Isoprene-OH Adduct 4: Initial conditions for nuclear velocity directions

5.000^a
0.909^b

1.500^a
0.909^b

0.333^a
0.200^b
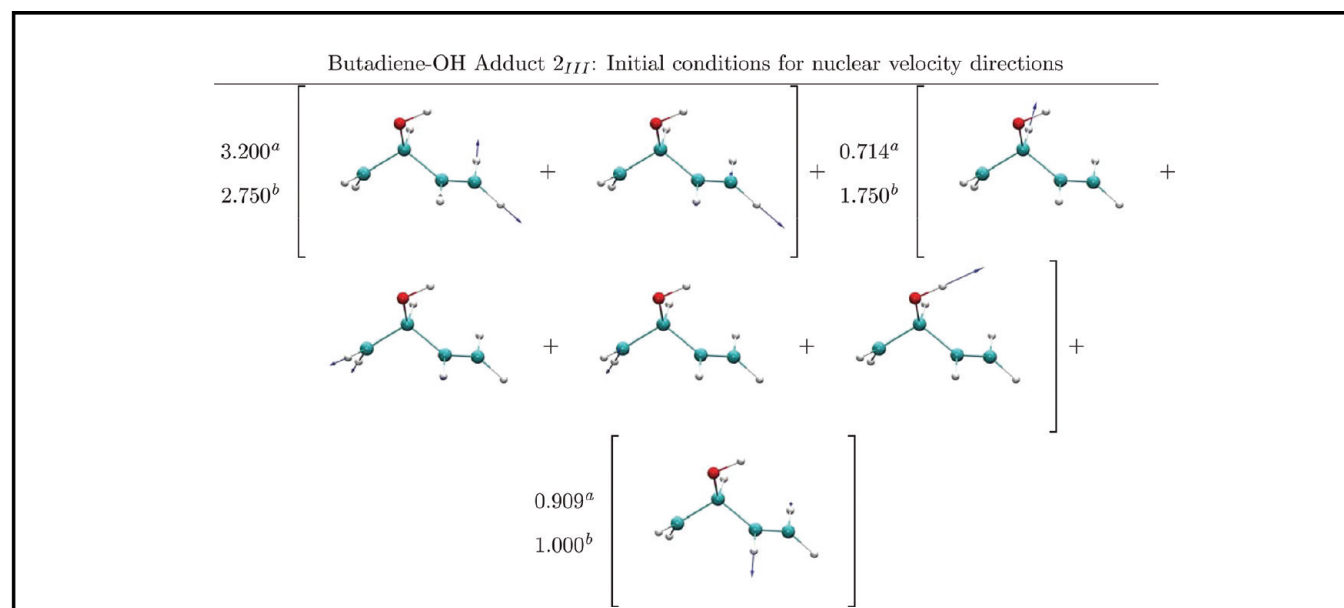
^{a}Simulation 4a. ^{b}Simulation 4b.

Table 8. Pumped Vibrational Modes for Butadiene–OH Adduct 1 (Vibrational Modes Represented with Arrows Proportional to the Harmonic Displacement Vectors)

Butadiene-OH Adduct 1: Initial conditions for nuclear velocity directions

3.800^a
1.1^b

1.000^a
1.000^b

1.750^a
1.000^b

^{a}Simulation 1a. ^{b}Simulation 1b.

3.2. Finite Temperature ab Initio Dynamics Simulations To Gauge the Effect of Energy Distribution on the Computed Vibrational Density of States.

In an experimental situation, such as that in ref 6, one might expect the adducts to be formed with greater energy in the OH and CO stretch modes. How does this energy get redistributed

Table 9. Pumped Vibrational Modes for Butadiene−OH, Simulation 2$_{II}$ (Vibrational Modes Represented with Arrows Proportional to the Harmonic Displacement Vectors)

Butadiene-OH Adduct 2$_{II}$: Initial conditions for nuclear velocity directions

^{a}Simulation 2$_{II^a}$. ^{b}Simulation 2$_{II^b}$.

Table 10. Pumped Vibrational Modes for Butadiene−OH, Simulation 2$_{III}$ (Vibrational Modes Represented with Arrows Proportional to the Harmonic Displacement Vectors)

Butadiene-OH Adduct 2$_{III}$: Initial conditions for nuclear velocity directions

^{a}Simulation 2$_{III^a}$. ^{b}Simulation 2$_{III^b}$.

through the other molecular modes and does this redistribution process have an effect on the vibrational density of states? Thus, to gauge the vibrational energy transfer, we carried out simulations using AIMD methodologies, ADMP,[6,8,19,21,22,25,26,40,45−48,52] and BOMD.[6,36−38] These simulations utilized the B3LYP hybrid density functional with double-ζ polarized-diffused 6-31+G-(d,p) basis, as suggested from previous studies[8,19−22,48,100,101] on similar systems. The simulations were conducted using the Gaussian series of electronic structure codes.[50]

To understand vibrational energy transfer, the initial conditions for the AIMD simulations were adjusted such that one obtained an asymmetric distribution of kinetic energies for

the individual atoms in the system. For this, the adduct molecules were divided into three fragments as shown in Figure 3. In the case of the isoprene adducts, the terminal methylene group to the left of the C−CH$_3$ in isoprene is labeled as fragment I, the vinyl group to the right is labeled as fragment II, and the C−CH$_3$ is designated as fragment III. The OH group maybe present on any of the fragments depending on the adduct being considered. This partitioning is depicted for isoprene−OH adduct 1 in Figure 3a. (Fragments I and II are shown in Figure 3a, but fragment III, the central region, has been omitted in the interest of clarity.) For consistency, the hydroxy−butadiene adducts are also subdivided in a similar fashion.
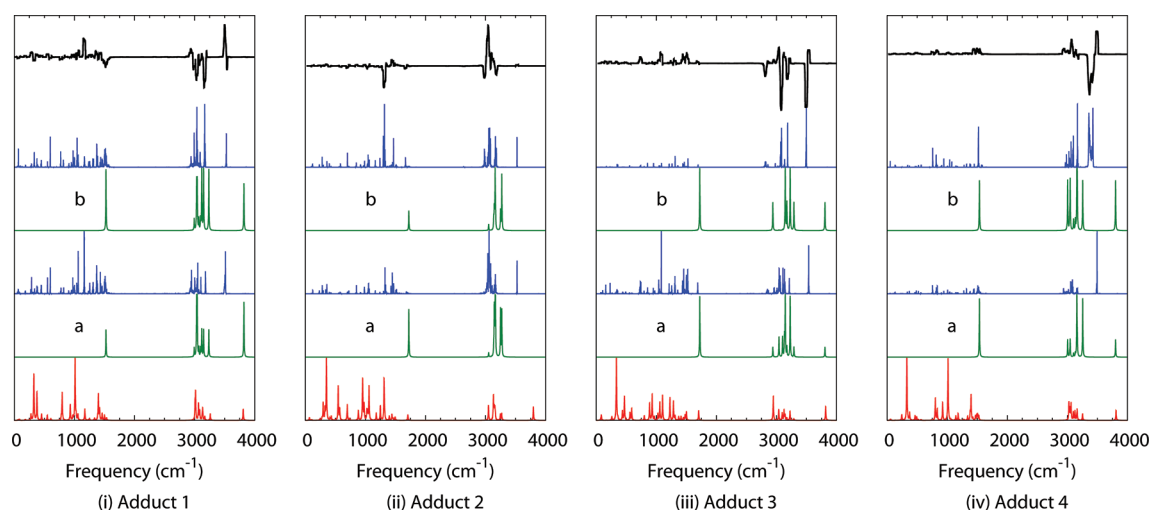
Figure 4. Comparison of IR spectrum obtained from harmonic frequency analysis (red curve) with the Fourier transform of the velocity−velocity autocorrelation function (eq 20, blue curve, obtained after 20 ps AIMD dynamics) with the initial energy distribution shown in the green curve for the four isoprene adducts. The red, blue, and green curves are normalized such that their respective maximum values are one. The label a (b) indicates that there is more energy in fragment I (II) compared to the other fragments. During the dynamics, the various vibrational modes couple with each other due to anharmonicity and energy is redistributed between the high-frequency stretching modes to the various bending and stretching modes, which depend on the amount of energy pumped initially. The difference in vibrational density of states between simulations I and II are shown in black. As noted in the text the effects are nontrivial between the two sets of simulations for each adduct.

That is, a terminal methylene group is labeled region I, a terminal vinyl group labeled II, and the C−H group is designated III. See Figure 3b for an illustration for adduct 1. In the first adduct, OH is present on the terminal methylene group while in the second adduct the OH is attached to the central C−H group. Using these fragments, OH can either be attached to fragment II or fragment III for the second butadiene adduct, thus providing two additional distinct sets of initial conditions for the dynamics of adduct 2. In this case, the two sets of simulations are referred to as adduct 2_{II} and adduct 2_{III}, respectively.

Time-resolved spectroscopy, also known as pump−probe spectroscopy, is a technique to investigate the energy transfer among modes in a molecule. This is done by exciting one or more modes of the molecule, either electronic, vibrational, or rotational, and probing the energy transferred to other modes. We simulate such a pump−probe technique here to investigate the role of energy redistribution and especially the sensitivity of the vibrational density of states to the initial conditions in dynamics. Again, we achieve this by providing an asymmetric distribution of initial kinetic energy to the molecule. In this case, we use a linear combination of the normal modes corresponding to the C−H and O−H stretches (obtained from harmonic frequency analysis) such that fragment III has the lowest total kinetic energy. That is, analogous to eq 22,

$$\vec{\mathcal{V}}(t=0) = \sum_{i} {}' C_i \vec{H}_i \qquad (32)$$

where the sum is constrained to include only the modes that result in the aforementioned asymmetric distribution of energy. Consequently we have two initial configurations for each adduct with either fragment I or fragment II with the higher kinetic energy at time $t = 0$. Thus, in our computational pump−probe scheme, we initially excite specific modes of the molecule and probe the amount of energy transferred into the remaining modes of the molecule. For convenience we label the simulations with more initial energy in fragment I as "a"

while the other as "b". The simulation parameters are given in Table 1. The precise modes that are excited at the beginning of each simulation can be found in Tables 4−10. The Appendix provides a short discussion to this effect. Furthermore, the resultant amount of "pumped energy" is listed in Table 2, for isoprene−OH, and Table 3, for butadiene−OH. In this fashion, we have locally controlled the initial amount of energy in neighborhood of the CO and OH bonds to facilitate the simulation of the experimental situation.

In Figure 4, the IR spectrum from harmonic frequency analysis (red) is compared with the initial distribution of energy supplied to the molecule (green), according to eq 32. The FT-VAC spectrum, obtained using eq 20 is also plotted in blue. These plots show that energy redistributes out of the initially pumped modes and onto other lower frequency modes. A measure of the time evolution of this energy redistribution is obtained from $I_V(\omega;t',t)$, and such an analysis is presented in Figure 5. Since the ab initio dynamics simulations explicitly account for anharmonicity through the sampling of the associated regions of the potential during dynamics, we find that the O−H stretch is red-shifted as a result of this anharmonicity. Compare the fact that the peaks corresponding to the OH stretch appear at ≈ 3800 cm^{-1} in the red and green curves in Figure 4, whereas this is red-shifted by a few hundred wavenumbers in the blue curves. In ref 9 we have demonstrated that the OH stretch is even more strongly perturbed through microsolvation by surrounding water molecules. Similar results were also noted in ref 6 for hydroxyl isoprene, in ref 8 for a peroxyl radical solvated in water, and in refs 19 and 21 for ions microsolvated in water. The anharmonicity which is largely noticeable in the O−H stretch results in coupling between the different harmonic modes leading to transfer of energy and stabilization of the adducts. The plots also indicate that the amount and mechanism of energy transfer depends on which fragments possess larger kinetic energy. This is true for all adducts studied, and *we note that the vibrational density of*
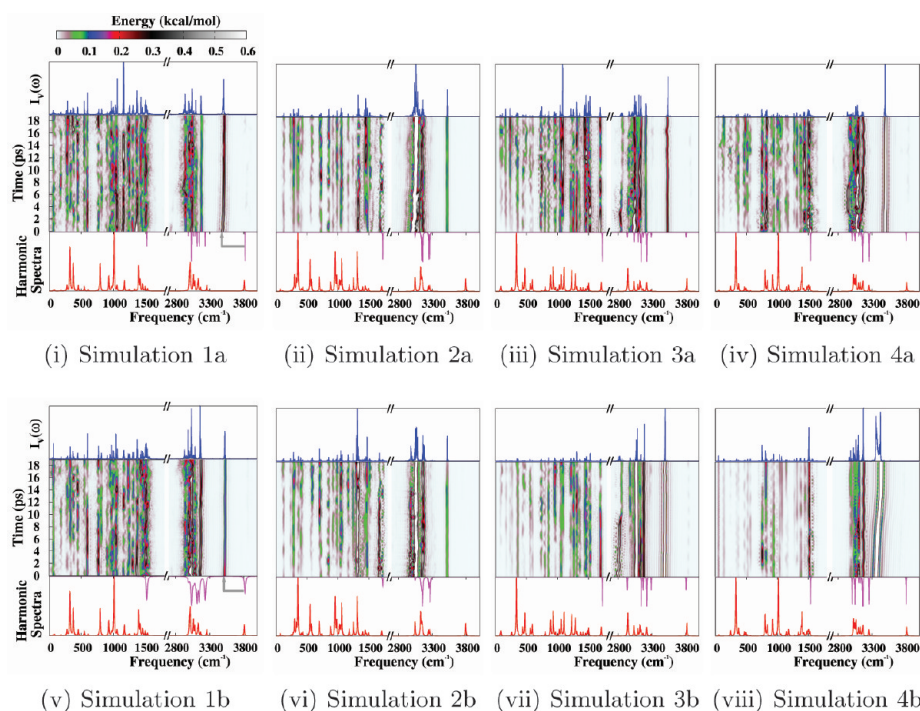
Figure 5. Isoprene–OH time-frequency correlation spectrum $I_V(\omega;t',t) \equiv \theta(t'';t,|t-t'|)$ (eq 24) where $\theta(t''; t, t')$ has been chosen as a step function that is equal to one inside $[t, t']$ and zero otherwise. Also $[t' - t] = 1$ ps, which makes $\theta(t''; t, |t - t'|)$ a function of (ω, t). The harmonic spectra are presented in red, the initial energy pumped states are in magenta, and $I_V(\omega)$ (eq 20) is shown in blue. For example, the pumped modes (magenta) in subfigure (i) are identical to the pumped modes shown in green in Figure 4i where region I has the greater energy. Similarly, the pumped modes (magenta) in subfigure (v) are identical to the pumped modes shown in green in Figure 4i where region II has the greater initial energy. The contour plot here depicts the energy reorganization pathway. The energy scale for the contour plot is presented on top of subfigure (i).
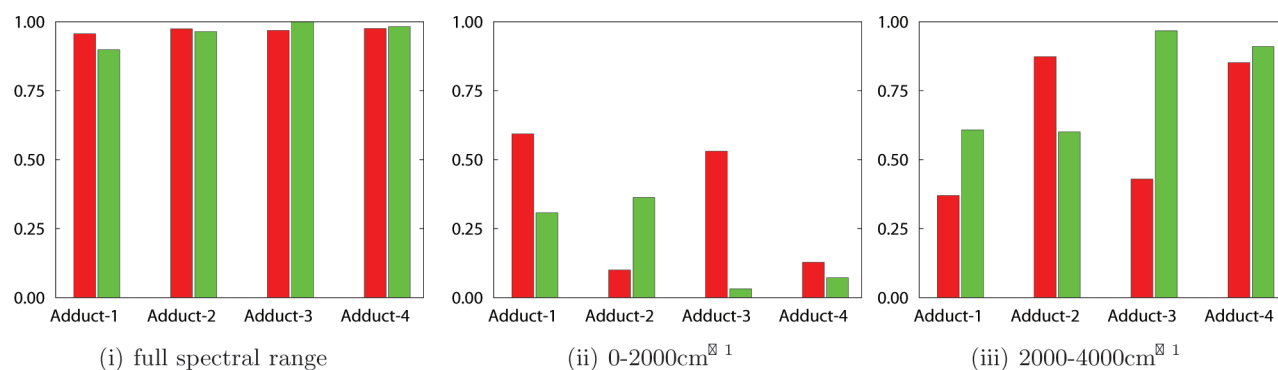

Figure 6. (i) Behavior of $\|J\|_2^2$ (see eqs 33 and 34) for hydroxy-isoprene simulation a (red) and simulation b (green) in the entire spectral range; (ii and iii) the same in the spectral ranges of 0−2000 and 2000−4000 cm^{-1}.

states (blue) depend on the initial conditions of the simulation (green).

On the basis of Figure 4, it is already clear that not only is there a critical difference in how the energy is redistributed for different initial conditions for a given adduct, as is indicated by the nonzero intensity of the black curves in Figure 4, these effects also vary between adducts. To quantify the effect of energy redistribution on the vibrational density of states, we introduce the parameter

$$\left\| J \right\|_2 \equiv \sqrt{\int d\omega \, |J(\omega)|^2} \tag{33}$$

where

$$J(\omega) = \hat{I}_V(\omega) - \hat{I}_{pumped}(\omega) \int d\omega' \hat{I}_V(\omega') \, \hat{I}_{pumped}(\omega') \tag{34}$$

In the preceding equation, $\hat{I}_V(\omega)$ and $\hat{I}_{pumped}(\omega)$ are normalized quantities defined as

$$\hat{I}_V(\omega) = I_V(\omega)/\|I_V\|_2 \tag{35}$$

$$\hat{I}_{pumped}(\omega) = I_{pumped}(\omega)/\left\|I_{pumped}\right\|_2 \tag{36}$$

where $\|I_V\|_2 = (\int d\omega (|I_V(\omega)|)^2)^{1/2}$ and $\|I_{pumped}\|_2 = (\int d\omega (|I_{pumped}(\omega)|)^2)^{1/2}$. The quantity $I_V(\omega)$ is defined in eq 20 and
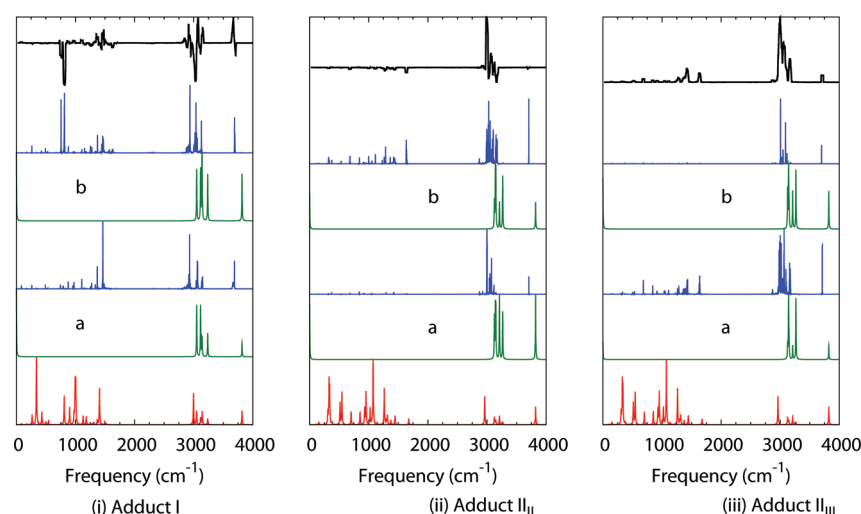
Figure 7. Comparison of IR spectrum obtained from harmonic frequency analysis (red curve) with the Fourier transform of the velocity−velocity autocorrelation function (eq 20, blue curve, obtained after AIMD dynamics) with the initial energy distribution shown in the green curve for the butadiene adducts. The red, blue, and green curves are normalized such that their respective maximum values are one. The label a (b) indicates that there is more energy in fragment I (II) compared to the other fragments, and the difference is shown in black, as in Figure 4.
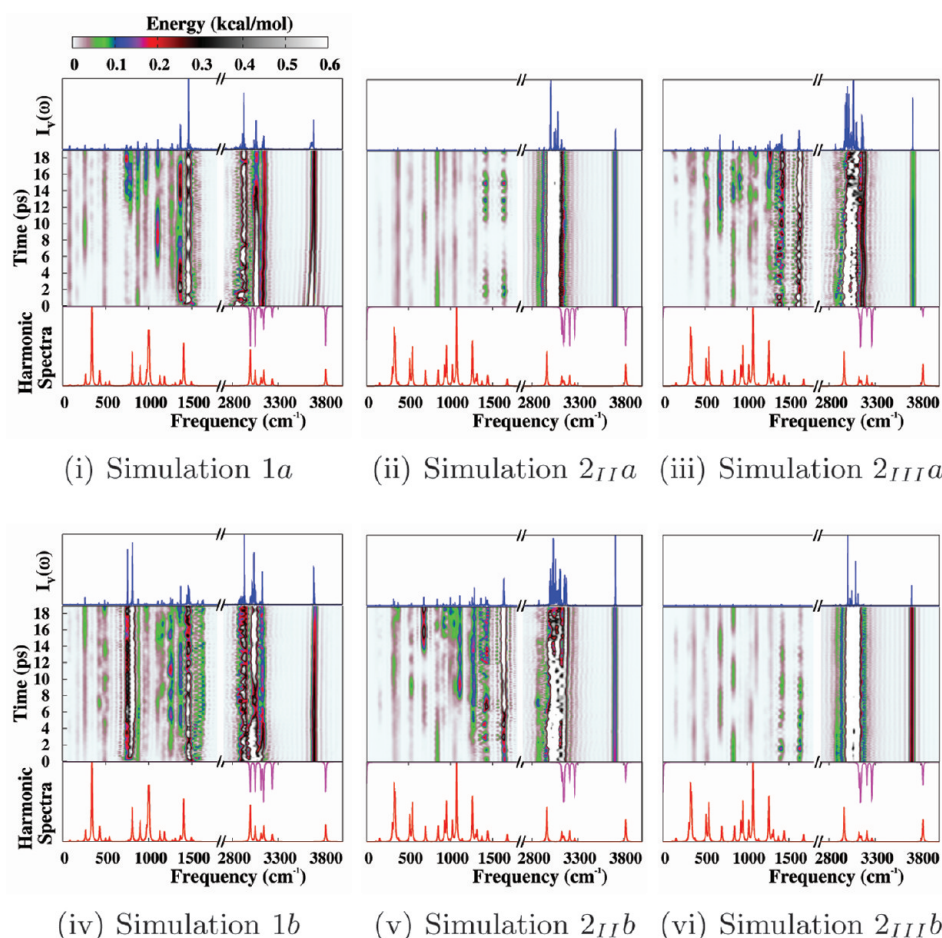

Figure 8. Butadiene−OH time-frequency correlation spectrum $I_V(\omega;t',t) \equiv \theta(t'';t,|t-t'|)$ (eq 24) where $\theta(t''; t, t')$ has been chosen as a step function that is equal to one inside $[t, t']$ and zero otherwise. Also $[t' - t] = 1$ ps, which makes $\theta(t'';t,|t-t'|)$ a function of (ω,t). The harmonic spectra are presented in red, the initial energy pumped states are in magenta, and $I_V(\omega)$ (eq 20) is shown in blue. For example, the pumped modes (magenta) in subfigure (i) are identical to the pumped modes shown in green in Figure 7i where region I has the greater energy. Similarly, the pumped modes (magenta) in subfigure (v) are identical to the pumped modes shown in green in Figure 7i where region II has the greater initial energy. The contour plot here depicts the energy reorganization pathway. The energy scale for the contour plot is presented on top of subfigure (i).
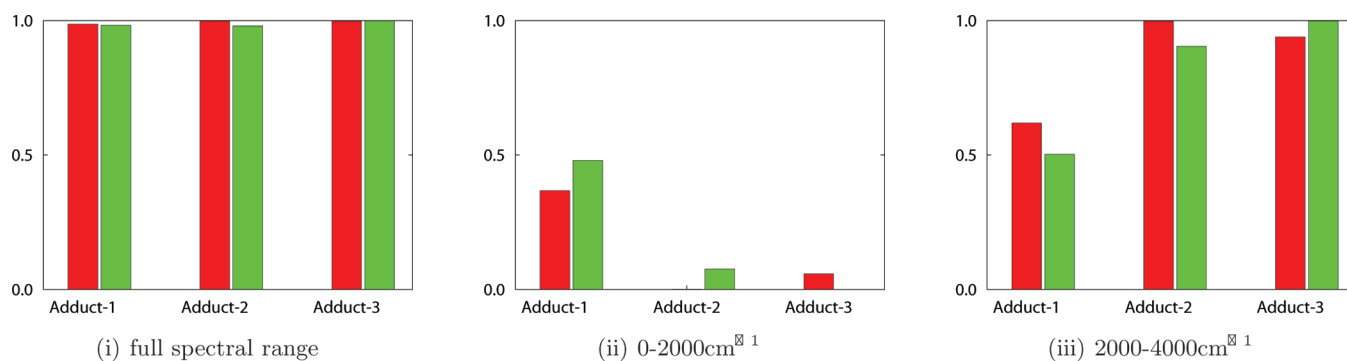
Figure 9. (i) Behavior of $\|J\|_2^2$ (see eqs 33 and 34) for hydroxy–butadiene simulation a (red) and simulation b (green) in the entire spectral range; (ii and iii) the same in the spectral ranges of 0−2000 and 2000−4000 cm^{-1}.
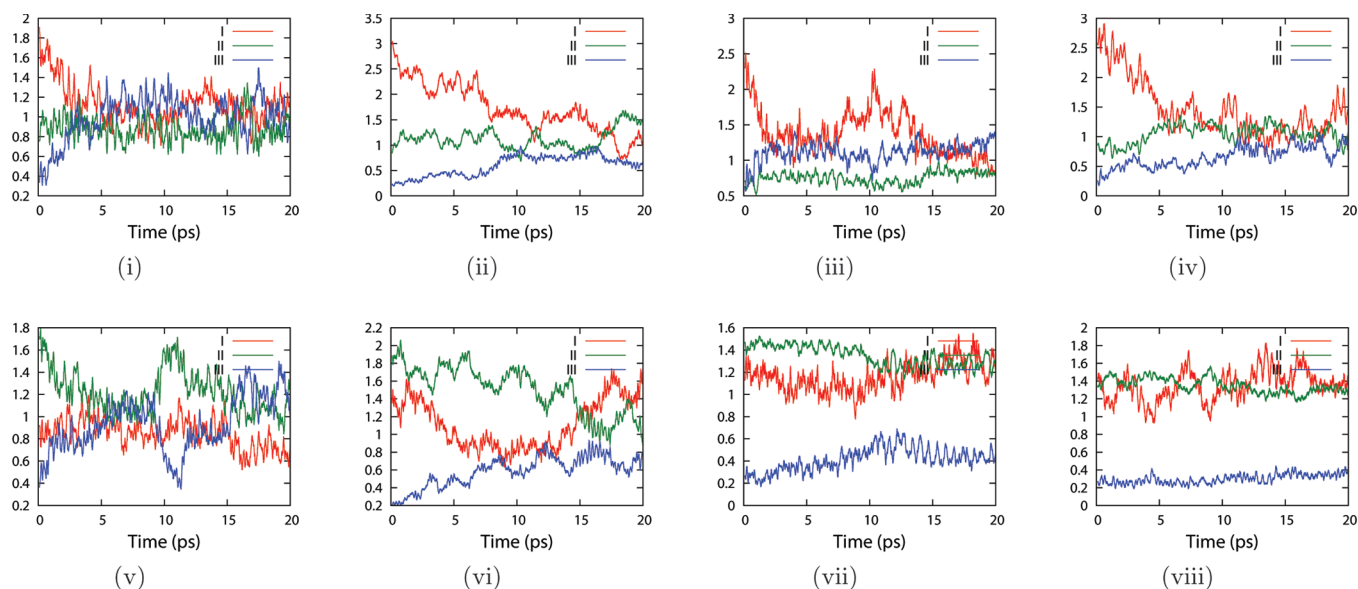

Figure 10. Equilibration of fragment energy for (i, v) adduct 1, (ii, vi) adduct 2, (iii, vii) adduct 3, and (iv, viii) adduct 4 for isoprene. The top panels correspond to configuration "a" while the bottom to configuration "b". The different fragments of adduct 1 equilibrate well compared to the other adducts.

is the (blue) vibrational density in Figure 4; $I_{pumped}(\omega)$ is the (green) pumped mode density in Figure 4. The term inside the integral on the right side in eq 34 may be interpreted as the spectral intensity in $I_V(\omega)$ that is common to the pumped intensity. As a result, since the vibrational density of states in eq 20 has units of velocity-squared, $\|J\|_2$ may be interpreted as a measure of *energy redistribution-flux*. In other words, the quantity $\|J\|_2$ represents the relative intensity of the vibrational density of states (represented in blue in Figure 4) orthogonal to the initial pumped modes (green in Figure 4).

The behavior of $\|J\|_2$ for the different isoprene simulations, in different spectral ranges, is provided in Figure 6. While Figure 6i shows little difference between the different adducts, there is a marked difference between adducts as well as for different initial conditions for a given adduct as seen in Figure 6ii,iii. Since the CO, CC stretch and bend modes are located below 2000 cm^{-1}, Figure 6ii indicates that while both simulations for adduct 1 have reasonable energy flux into the low-frequency modes, this is not the case for adducts 2−4. This is also noted from the relatively lower levels of flux for adduct 1 in Figure 6iii.

Thus, energy redistribution is not uniform in these adducts during the length of these simulations.

A similar analysis of the hydroxy butadiene adducts in Figures 7−9 also indicates a significant reduction in flux toward the lower frequency states. (See Figure 9iii.) But the cumulative flux of all adducts toward these lower frequency states appears to be even lower for butadiene than was found to be the case for isoprene. The relative intensities of the histgram plots in Figure 9ii should be compared to those found in Figure 6ii. While these factors clearly affect the vibrational density of states, one must keep in mind that these simulations were constructed in the product channel, that is, the product of the isoprene−OH and butadiene−OH adduct reactive steps. Future simulations conducted at or near the transition states of these reactions will yield insight into the direct effect of these energy-transfer propensities on the reaction rates. Future studies will also include the effect of these energy flow differences into the density of states as required in RRKM theory.

3.2.1. Role of Anharmonicity on Energy Redistribution. Before we conclude this section, we show that energy redistributions similar to those encountered above can only be
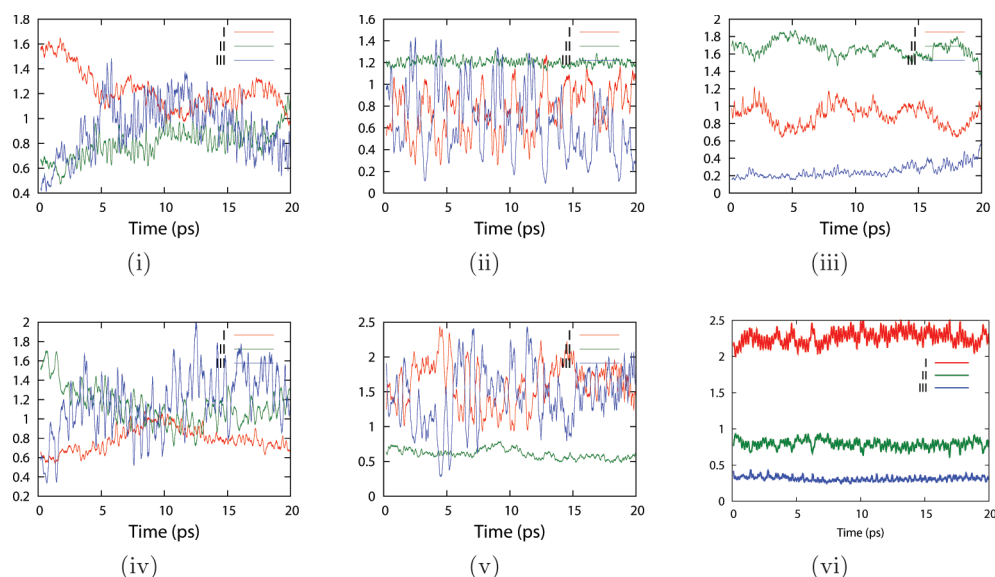
Figure 11. Equilibration of fragment energy for (i, iv) adduct 1, (ii, v) adduct 2_{II}, and (iii,vi) adduct 2_{III} for butadiene. The top panels correspond to configuration "a" while the bottom to configuration "b". The different fragments of adduct 1 equilibrate well compared to the other adducts.
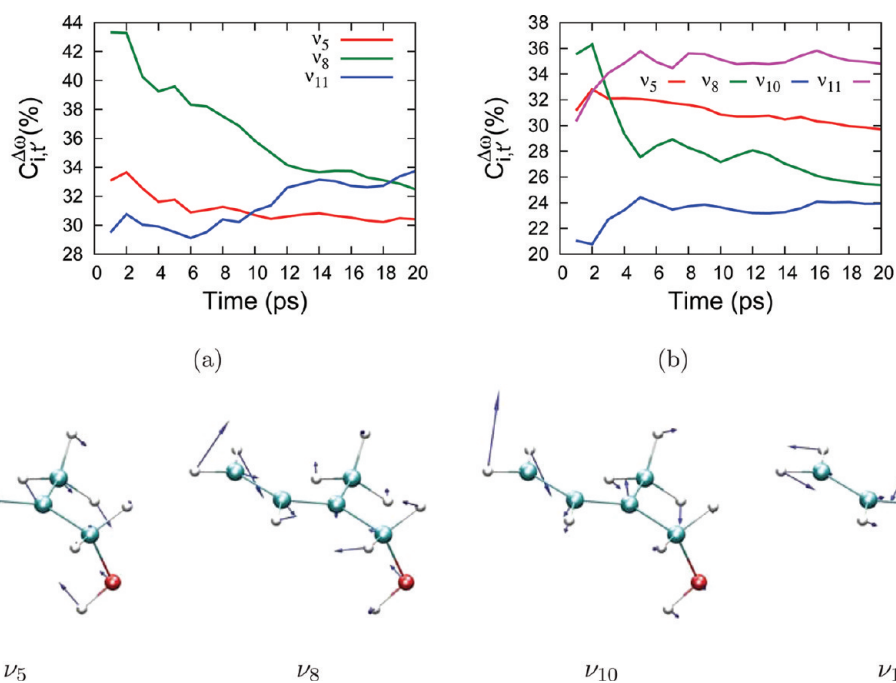

Figure 12. t'-dependent evolution of the harmonic components, $C_{i,t'}^{\Delta\omega}$, of the isoprene−OH adducts (a) 1a and (b) 1b in the frequency range of $\Delta\omega = 1200-1800$ cm^{-1}. The contributing modes are shown right below.

obtained when the potential energy surface is constructed beyond the harmonic approximation. In our case, the fully coupled anharmonic potential surface is constructed through explicit on-the-fly computation of the surface and its gradients as required in section 2. (See eqs 8−11)

When a harmonic approximation is invoked through a frequency calculation constructed at a local minimum, the nuclear equations of motion in eq 6 become separable for each degree of freedom:

$$\frac{d^2\mathbf{Q}_i}{dt^2} = -k_i\mathbf{Q}_i \tag{37}$$

where $\{\mathbf{Q}_i\}$ are the set of mass-weighted harmonic modes obtained from diagonalization of the electronic structure Hessian matrix and $\{k_i\}$ are the associated set of eigenvalues or force constants. Due to the separable form of eq 37, achieved from the lack of coupling between the modes, $\{\mathbf{Q}_i\}$, as part of the harmonic approxmation, the nuclear equations of motion derived from using eqs 8 and 10 remain independent for the various degrees of freedom. Consequently the pumped modes will retain their energy and there will be no dissipation into the remaining set of modes. Such an energy redistribution is only possible here because the (anharmonic) potential surface is fully coupled (that is, nonseparable) and computed explicitly.
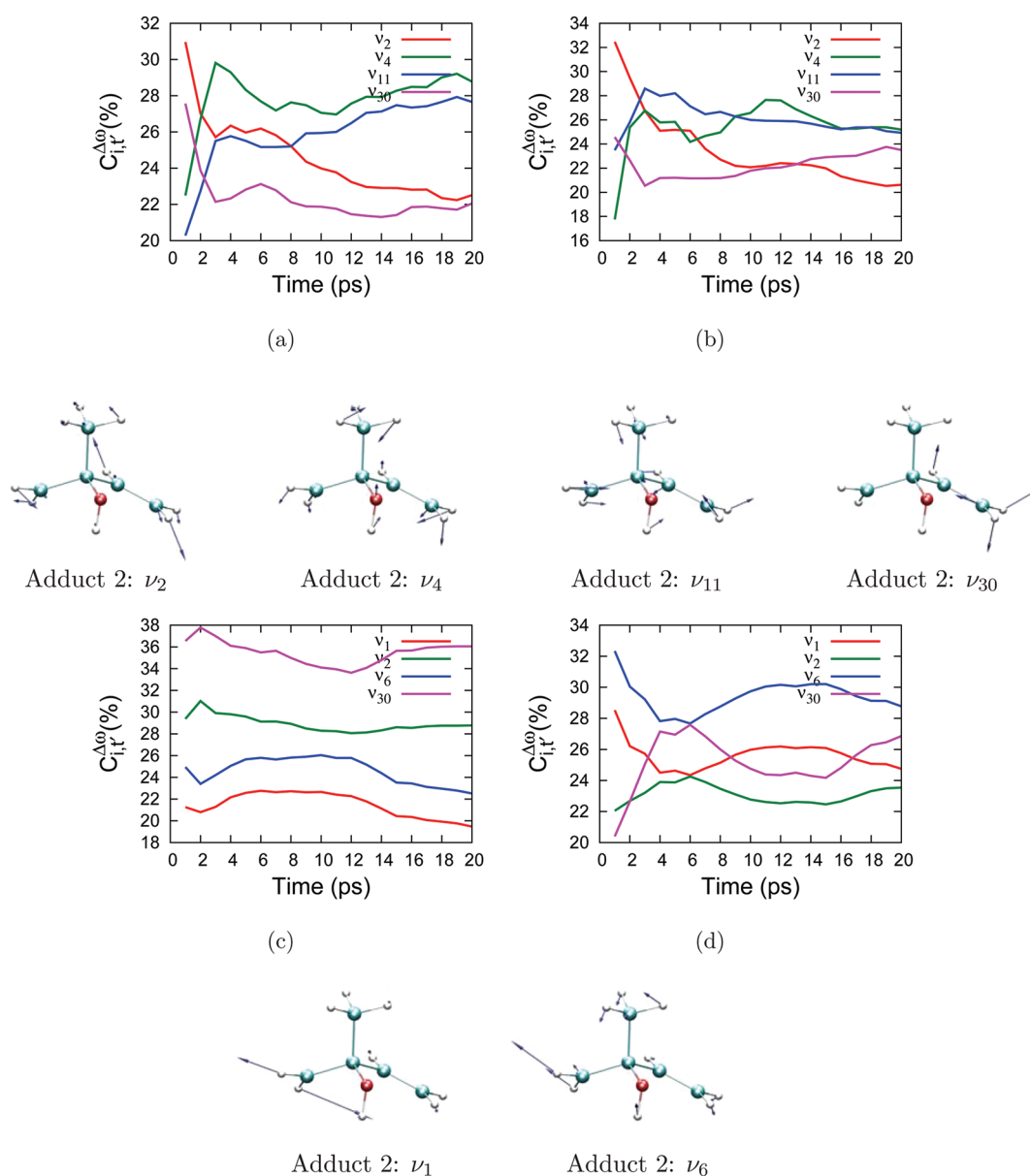
(a)

(b)

Adduct 2: ν_2 Adduct 2: ν_4 Adduct 2: ν_{11} Adduct 2: ν_{30}

(c)

(d)

Adduct 2: ν_1 Adduct 2: ν_6

Figure 13. t'-dependent evolution of the harmonic components, $C_{i,t'}^{\Delta\omega}$, of the isoprene−OH adduct 2a in the frequency ranges ($\Delta\omega$) of (a) 0−1200 and (b) 1200−1800 cm^{-1} and adduct 2b in the frequency ranges ($\Delta\omega$) of (c) 0−1200 and (d) 1200−1800 cm^{-1}. The contributing modes are also displayed.

Thus far we analyzed the cumulative effect of energy redistribution. Next, we consider the time dependence of energy redistribution by estimating the equilibration time for kinetic energy in the different fragments.

3.3. Equilibration of Fragment Kinetic Energy for Each Adduct. The three fragments start with different kinetic energies and equilibrate during the simulations, via transfer of energy between the vibrational modes. In Figures 10 and 11, we present the time evolution of a kinetic energy quotient which is defined as the ratio of the kinetic energy per atom for each fragment to the kinetic energy per atom of the whole molecule. This quotient has the physical interpretation that when it is equal to one, the average kinetic energy in the fragment is equal to that in the molecule.

For isoprene adduct 1, we observe that the three fragments equilibrate within a 5 ps time scale. There is a difference between the energy flow depending on which fragment has the

larger energy. For adduct 1, simulation "a", the kinetic energy appears to be equilibrated at 5 ps. For simulation "b", energy is constantly redistributed leading to greater fluctuations in the energy of the three fragments. However, clearly the energy relaxation process appears to be far slower for adducts 2, 3, and 4, and also very different across simulations for the same adduct, which appears to be consistent with the difference in vibrational density of states seen in the previous section. In a similar fashion, Figure 11 shows that the butadiene adduct 1 also appears to equilibrate faster as compared to the other adducts. This is also consistent with the larger amplitude of the difference density of states (black curve) in the lower frequency end of Figure 7 for the butadiene adduct 1 simulations as compared to adduct 2. Also see Figure 9ii.

3.4. Spectral Analysis of Energy Transfer. In the two previous subsections we probed the evolution of energy as a function of different pumped modes. In the current section we
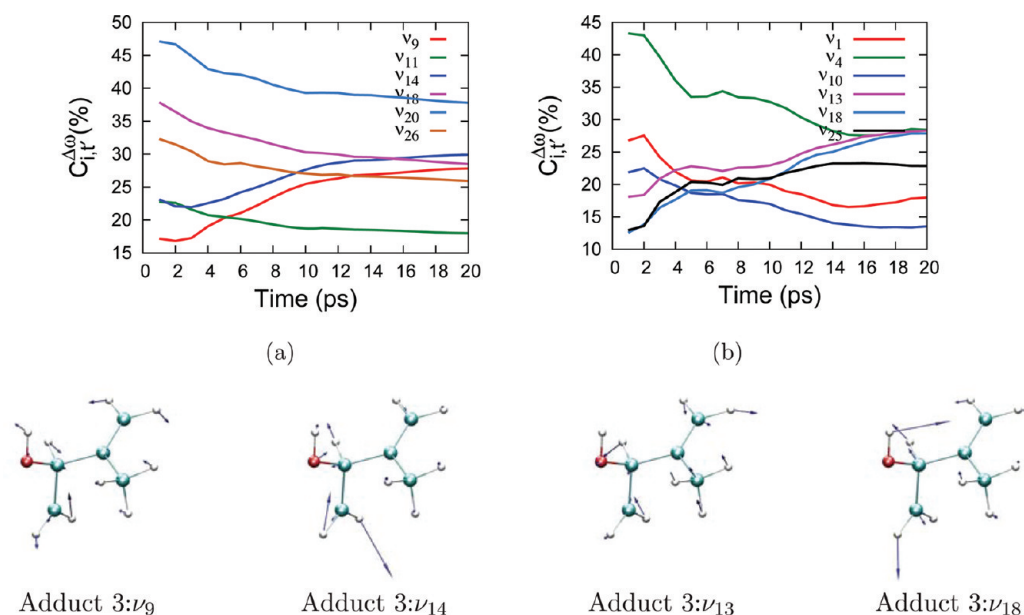
Q

dx.doi.org/10.1021/jp212330e | J. Phys. Chem. A XXXX, XXX, XXX−XXX

Figure 14. t'-dependent evolution of the harmonic components, $C_{i,t}^{\Delta\omega}$, of the isoprene−OH adducts (a) 3a in the frequency range of $\Delta\omega = 2600-3400$ cm^{-1} and (b) 3b in the frequency range of $\Delta\omega = 0-1200$ cm^{-1} and the corresponding 2D spectra for adducts (c) 3a and (d) 3b.
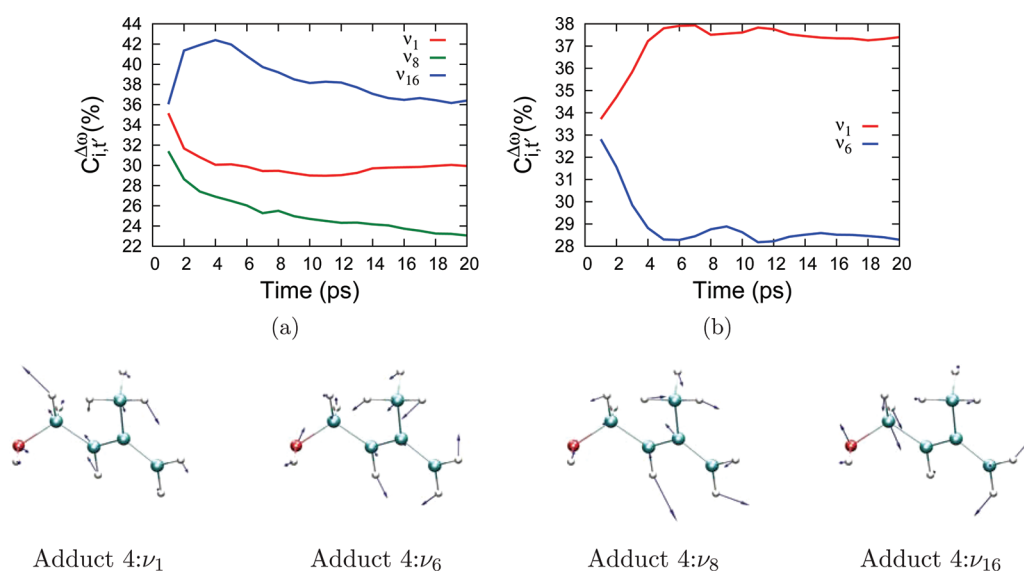

Figure 15. t'-dependent evolution of the harmonic components, $C_{i,t}^{\Delta\omega}$, of the isoprene−OH adducts (a) 4a and (b) 4b in the frequency range of $\Delta\omega = 2600-3400$ cm^{-1} and the corresponding corresponding 2D spectra for adducts (c) 4a and (d) 4b.

evaluate the harmonic modes that are involved in such an energy reorganization process to provide a possible mechanism for energy transfer and explain the differences seen in the previous sections. (We reiterate that the precise modes that are excited at the beginning of each simulation can be found in Tables 4−10. The resultant amount of "pumped energy" is listed in Table 2, for isoprene−OH, and Table 3, for butadiene−OH.) We present an analysis of the dynamically averaged vibrational density of states presented in section 3.2, using the harmonic mode decomposition scheme, eq 26 in section 2.2. This scheme essentially allows us to analyze the differences in the vibrational energy density by studying contributions from the fundamental harmonic modes.

In Figure 4, the FT-VAC is normalized with respect to the largest intensity. The figure shows two distinct spectral regions: 2600−3800 cm^{-1} consists of the C−H and O−H stretch frequencies and 0−1800 cm^{-1} consists of the bending, torsional, and C−C, C−O stretching vibrations. These spectra include anharmonic contributions and display a flow of energy from the C−H and O−H stretching frequencies in the range of 1800− 3800 cm^{-1} to the torsional and C−C, C−O stretching vibra- tions at frequencies below 1800 cm^{-1}. This is noted by comparison with the modes that are initially excited during dynamics, as seen in Figure 4. We carry out our harmonic mode analysis by partitioning the spectral regions further as follows: (a) the 3400−3800 cm^{-1} range corresponding to the OH stretch, (b) 2600−3400 cm^{-1}, corresponding to the C−H stretches, (c) 1200−1800 cm^{-1}, which corresponds mostly to the region containing the C−C stretches and some bending modes, and (d) 0−1200 cm^{-1}, the remaining region which contains the CO stretch mode. In this section we direct our attention toward the redistribution in the 0−1200 and 1200−1800 cm^{-1} regions.

In Figures 12−15, we provide the evolution of the $C_{i,T}^{\Delta\omega}$ (eq 26) coefficients in the given frequency range.

We first analyze the case for isoprene adduct 1. In Figure 12, we present the evolution of the most dominant modes for the two isoprene adduct 1 simulations in the 1200−1800 cm^{-1} range. We have already noted[6] that energy exchange involves the open jaw motion of the five-membered O−C−C−C−H ring. The corresponding IR intensity scaled contribution ($D_{i,t}^{\Delta\omega}$ in eq 27) however shows this frequency region to be dominated by the CO stretch mode and hydroxyl and methyl proton wag modes. Simulation 1b shows exchange of energy between two modes ν_8 and ν_{10} (see Figure 12) involving the in-plane bend of the C−C backbone coupled to the symmetric stretch of the C−C bonds in the five-membered ring with the open jaw motion of the five-membered ring. In simulation 1a, we note that energy leaks out of the open jaw motion of the five-membered ring (ν_8) into the C−C backbone of isoprene continuously while, in simulation 1b, there is initially energy leaking out with a time scale of 4 ps and then exchanges back and forth between the two different types of modes with a time scale of 2 ps. This appears to be consistent with the evolution of fragment kinetic energies seen in section 3.2, and there is substantial energy exchange between the modes involved in adduct 1. Comparing the mode contribution for both adduct 1 simulations, it is evident that the modes involved in energy exchange are the same, which indicates that equilibration may have occurred during the course of the simulation. The similarity in energy redistribution pathways is unique to the adduct 1 simulations, which is again consistent with the results found in the previous sections.

In Figure 13, we present the time evolution of the most dominant modes for isoprene adduct 2 in two different frequency ranges. The modes ν_i, i = 2, 4, 6, 11, correspond to the various torsional modes of the C−C backbone, ν_1 corresponds to the antisymmetric wag of H attached to the methylene carbon (fragment 1), and ν_{30}, which was initially excited, corresponds to the C═C stretch of the vinyl group. In the lower frequency region, the energy exchange occurs via similar pathways, i.e., between the torsional modes of the C−C backbone and the initially excited C═C stretch of the vinyl group. In the frequency range $\Delta\omega$ = 1200−1800 cm^{-1}, adduct 2, simulation a, shows very little energy exchange (<4%) compared to simulation 2b, where there is energy exchange between the torsional modes and the C═C backbone. Adduct 2 which has the OH group attached to a tertiary carbon atom is sterically hindered due to the bulky methyl group, and hence the torsional modes become important for energy exchange.

Figures 14 and 15 show the evolution of the most dominant modes for adducts 3 and 4, respectively. As stated earlier, the modes responsible for energy transfer depend on which fragment of the molecule was initially excited. As stated earlier, adduct 1 shows a similar evolution of energy in the different modes due to the five-membered ring. We conclude that the five-membered ring brings about stability in isoprene adduct 1 due to increased energy repartitioning into the modes that comprise the ring structure. Since such a ring structure is absent in adducts 2 and 3, the adducts are less stable. Adduct 4 can form a six-membered ring; however, such a structure does not correpond to the global minimum.

4. CONCLUSION

In this publication, the "pump−probe" atom-centered density matrix propagation, originally introduced in ref 6, is utilized to probe energy redistribution in atmospheric reaction intermediates. In ref 6, we investigated the difference in energy-transfer pathways in 1-hydroxy isoprene and 1-hydroxy butadiene. We showed that the difference in stability of these two H-bonded reaction intermediates is due to the formation of a stable five-membered ring in hydroxy isoprene. Here the stability of reaction intermediates of all hydroxyl radical adducts to isoprene (four adducts) and butadiene (three adducts) molecules are used as a case study to develop novel computational techniques involving "pump−probe" ab initio molecular dynamics.

The dynamics results are analyzed by considering multiple factors. (a) The density of states encountered during the dynamics trajectories is computed as a function of different "probed" populations for initial vibrational states. This is tailored to mimic the manner in which samples may be prepared during the experimental situation. For example, the molecular region encompassing the bond formed due to addition of OH radical to isoprene and 1,3-butadiene may be populated with greater (or lesser) energy and the associated difference in vibrational energy density computed to ascertain the extent of energy redistribution. We monitor the energy redistribution flux obtained from the vibrational density and infer significant differences in the way the energy is redistributed among the modes (as a result of anharmonicity) for different initial state preparation schemes and for the different adducts. (b) The energy redistribution process is quantified by computing two-dimensional time-frequency correlation functions to provide the temporal evolution of energy populations in various frequency domains. (c) At an additional level, the kinetic energy localized in different portions of the molecule is considered as a function of time. (d) Finally the amount of energy localized in each harmonic mode is computed as a function of time. This analysis provides a possible energy-transfer mechanism that explains the differences in energy redistribution.

The results here essentially underline the fact that energy redistribution pathways may have a significant role on the density of states. The redistribution here is almost completely governed by anharmonicity as sampled during the ab initio molecular dynamics simulations. In addition to the role of anharmonicity seen here, in ref 9 the effects in the vibrational density were shown to be quite significant in the presence of water. In future publications these effects will be evaluated for the peroxyl radicals and also used in computing estimates for the vibrational density of states required in the RRKM rate expression.

■ APPENDIX: DESCRIPTION OF THE MODES THAT WERE INITIALLY PUMPED DURING THE SIMULATIONS

As noted in section 3.2, eq 32,

$$\vec{v}(t=0) = \sum_i {}'C_i\vec{H}_i \tag{A1}$$

the harmonic modes are selectively pumped during the pump−probe AIMD simulations. The goal of this selective process was to administer different amounts of energy in the various fragments for hydroxy−isoprene and hydroxy−butadiene, with fragments described in Figure 3, and associated discussion in section 3.2. The energy redistribution was then studied in

section 3.2. Here, we provide a description of the actual modes that were simulated during the initial portion of each dynamics calculation. The modes are presented in Tables 4–10. Furthermore, the resultant amount of "pumped energy" is listed in the main text of the paper. See Table 2 for isoprene–OH and Table 3 for butadiene–OH.

As can be seen from the tables in the main text, the modes selectively stimulated here do indeed provide a differential energy distribution for the calculations.

■ AUTHOR INFORMATION

Corresponding Author
*E-mail: iyengar@indiana.edu.

Notes
The authors declare no competing financial interest.

■ ACKNOWLEDGMENTS

■ REFERENCES

(1) Sillman, S. *Annu. Rev. Energy Environ.* **1993**, *18*, 31–56.

(2) Heard, D. E.; Pilling, M. J. *Chem. Rev.* **2003**, *103*, 5163–5198.

(3) Tan, D.; Faloona, I.; Simpas, J. B.; Brune, W.; Shepson, P. B.; Couch, T. L.; Sumner, A. L.; Carroll, M. A.; Thornberry, T.; Apel, E.; Riemer, D.; Stockwell, W. *J. Geophys. Res., [Atmos.]* **2001**, *106*, 24407–24427.

(4) Carslaw, N.; Creasey, D. J.; Harrison, D.; Heard, D. E.; Hunter, M. C.; Jacobs, P. J.; Jenkin, M. E.; Lee, J. D.; Lewis, A. C.; Pilling, M. J.; Saunders, S. M.; Seakins, P. W. *Atmos. Environ.* **2001**, *35*, 4725–4737.

(5) Guenther, A. *Nature* **2008**, *452*, 701–702.

(6) Vimal, D.; Pacheco, A. B.; Iyengar, S. S.; Stevens, P. S. *J. Phys. Chem. A* **2008**, *112*, 7227–7237.

(7) Peeters, J.; Nguyen, T. L.; Vereecken, L. *Phys. Chem. Chem. Phys.* **2009**, *11* (28), 5935–5939.

(8) Iyengar, S. S. *J. Chem. Phys.* **2005**, *123*, No. 084310.

(9) Dietrick, S. M.; Pacheco, A. B.; Phatak, P.; Stevens, P. S.; Iyengar, S. S. *J. Phys. Chem. A* **2012**, *116*, 399–414.

(10) Aloisio, S.; Francisco, J. S. *Acc. Chem. Res.* **2000**, *33*, 825–830.

(11) Aloisio, S.; Francisco, J. S. *J. Phys. Chem. A* **1998**, *102*, 1899–1902.

(12) Shi, Q.; Belair, S. D.; Francisco, J. S.; Kais, S. *Proc. Natl. Acad. Sci. U. S. A.* **2003**, *100* (17), 9686–9690.

(13) Clark, J.; Call, S. T.; Austin, D. E.; Hansen, J. C. *J. Phys. Chem. A* **2010**, *114*, 6534–6541.

(14) Vaida, V. *J. Chem. Phys.* **2011**, *109*, No. 020901.

(15) Jung, Y.; Marcus, R. A. *J. Am. Chem. Soc.* **2007**, *129*, 5492–5502.

(16) Mantz, Y.; Geiger, F. M.; Molina, L. T.; Molina, M. J.; Trout, B. L. *J. Phys. Chem. A* **2001**, *105*, 7037–7046.

(17) Aplincourt, P.; Anglada, J. M. *J. Phys. Chem. A* **2003**, *107*, 5798–5811.

(18) Aplincourt, P.; Anglada, J. M. *J. Phys. Chem. A* **2003**, *107*, 5812–5820.

(19) Iyengar, S. S. *J. Chem. Phys.* **2007**, *126*, No. 216101.

(20) Iyengar, S. S.; Petersen, M. K.; Day, T. J. F.; Burnham, C. J.; Teige, V. E.; Voth, G. A. *J. Chem. Phys.* **2005**, *123*, No. 084309.

(21) Li, X.; Teige, V. E.; Iyengar, S. S. *J. Phys. Chem. A* **2007**, *111*, 4815–4820.

(22) Iyengar, S. S.; Day, T. J. F.; Voth, G. A. *Int. J. Mass Spectrom.* **2005**, *241*, 197–204.

(23) Iyengar, S. S.; Li, X.; Sumner, I. *Adv. Quantum Chem.* **2008**, *55*, 333–353.

(24) Sumner, I.; Iyengar, S. S. *J. Phys. Chem. A* **2007**, *111*, 10313–10324.

(25) Li, X.; Moore, D. T.; Iyengar, S. S. *J. Chem. Phys.* **2008**, *128*, 184308.

(26) Li, X.; Oomens, J.; Eyler, J. R.; Moore, D. T.; Iyengar, S. S. *J. Chem. Phys.* **2010**, *132*, 244301.

(27) Diken, E. G.; Headrick, J. M.; Roscioli, J. R.; Bopp, J. C.; Johnson, M. A.; McCoy, A. B. *J. Phys. Chem. A* **2005**, *109*, 1487–1490.

(28) Iyengar, S. S.; Sumner, I.; Jakowski, J. *J. Phys. Chem. B* **2008**, *112*, 7601–7613.

(29) Nguyen, T. L.; Barker, J. R. *J. Phys. Chem. A* **2010**, *114*, 3718–3730.

(30) Nguyen, T. L.; Stanton, J. F.; Barker, J. R. *Chem. Phys. Lett.* **2010**, *409*, 9–15.

(31) Miller, W. H. *Faraday Discuss.* **1998**, 1–21.

(32) Bowman, J. M. *Acc. Chem. Res.* **1986**, *19*, 202–208.

(33) Jung, J. O.; Gerber, R. B. *J. Chem. Phys.* **1996**, *105*, 10332–10348.

(34) Iyengar, S. S. *Int. J. Quantum Chem.* **2009**, *109*, 3798–3810.

(35) Wang, I. S. Y.; Karplus, M. *J. Am. Chem. Soc.* **1973**, *95*, 8160–8164.

(36) Leforestier, C. *J. Chem. Phys.* **1978**, *68*, 4406–4410.

(37) Bolton, K.; Hase, W. L.; Peslherbe, G. H. Direct Dynamics of Reactive Systems. *Modern Methods for Multidimensional Dynamics Computations in Chemistry*; World Scientific: Singapore, 1998; p 143.

(38) Payne, M. C.; Teter, M. P.; Allan, D. C.; Arias, T. A.; Joannopoulos, J. D. *Rev. Mod. Phys.* **1992**, *64*, 1045–1097.

(39) Deumens, E.; Diz, A.; Longo, R.; ÖHrn, Y. *Rev. Mod. Phys.* **1994**, *66*, 917–983.

(40) Schlegel, H. B.; Millam, J. M.; Iyengar, S. S.; Voth, G. A.; Daniels, A. D.; Scuseria, G. E.; Frisch, M. J. *J. Chem. Phys.* **2001**, *114*, 9758–9763.

(41) Marx, D.; Hutter, J. Ab Initio Molecular Dynamics: Theory and Implementation. *Modern Methods and Algorithms of Quantum Chemistry*, Vol. *1*; John Vonneumann Institute for Computing: Julich, Germany, 2000; pp 301–449.

(42) Schlegel, H. B. *J. Comput. Chem.* **2003**, *24*, 1514–1527.

(43) Iyengar, S. S.; Jakowski, J. *J. Chem. Phys.* **2005**, *122*, 114105.

(44) Martinez, T. J.; BenNun, M.; Ashkenazi, G. *J. Chem. Phys.* **1996**, *104*, 2847–2856.

(45) Iyengar, S. S.; Schlegel, H. B.; Millam, J. M.; Voth, G. A.; Scuseria, G. E.; Frisch, M. J. *J. Chem. Phys.* **2001**, *115*, 10291–10302.

(46) Schlegel, H. B.; Iyengar, S. S.; Li, X.; Millam, J. M.; Voth, G. A.; Scuseria, G. E.; Frisch, M. J. *J. Chem. Phys.* **2002**, *117*, 8694–8704.

(47) Iyengar, S. S.; Schlegel, H. B.; Voth, G. A.; Millam, J. M.; Scuseria, G. E.; Frisch, M. J. *Isr. J. Chem* **2002**, *42*, 191–202.

(48) Iyengar, S. S.; Frisch, M. J. *J. Chem. Phys.* **2004**, *121*, 5061–5070.

(49) Iyengar, S. S.; Schlegel, H. B.; Voth, G. A. *J. Phys. Chem. A* **2003**, *107*, 7269–7277.

(50) Frisch, M. J.; Trucks, G. W.; Schlegel, H. B.; Scuseria, G. E.; Robb, M. A.; Cheeseman, J. R.; Montgomery, J. A., Jr.; Vreven, T.; Kudin, K. N.; Burant, J. C. et al. *Gaussian 03*, Revision b.02; Gaussian: Pittsburgh, PA, 2003.

(51) Rega, N.; Iyengar, S. S.; Voth, G. A.; Schlegel, H. B.; Vreven, T.; Frisch, M. J. *J. Phys. Chem. B* **2004**, *108*, 4210–4220.

(52) Pavone, M.; Biczysko, M.; Rega, N.; Barone, V. *J. Phys. Chem. A* **2010**, *114*, 11509–11514.

(53) Car, R.; Parrinello, M. *Phys. Rev. Lett.* **1985**, *55*, 2471–2474.

(54) Remler, D. K.; Madden, P. A. *Mol. Phys.* **1990**, *70*, 921–966.

(55) Tuckerman, M. E.; Parrinello, M. *J. Chem. Phys.* **1994**, *101*, 1302–1315.

(56) Andersen, H. C. *J. Chem. Phys.* **1980**, *72*, 2384–2393.

(57) Parrinello, M.; Rahman, A. *Phys. Rev. Lett.* **1980**, *45*, 1196–1199.

(58) Petersen, M. K.; Iyengar, S. S.; Day, T. J. F.; Voth, G. A. *J. Phys. Chem. B* **2004**, *108*, 14804–14806.

(59) Petersen, P. B.; Saykally, R. J. *J. Phys. Chem. B* **2005**, *109*, 7976–7980.

(60) Levering, L. M.; Sierra-Hernandez, M. R.; Allen, H. C. *J. Phys. Chem. C* **2007**, *111*, 8814–8826.

(61) Petersen, P. B.; Saykally, R. J. *Annu. Rev. Phys. Chem.* **2006**, *57*, No. 333364.

(62) Buch, V.; Milet, A.; Vacha, R.; Jungwirth, P.; Devlin, J. P. *Proc. Natl. Acad. Sci. U. S. A.* **2007**, *104*, 7342−7347.

(63) Morrone, J. A.; Hasllinger, K. E.; Tuckerman, M. E. *J. Phys. Chem. B* **2006**, *110*, 3712−3720.

(64) Mucha, M.; Frigato, T.; Levering, L. M.; Allen, H. C.; Tobias, D. J.; Dang, L. X.; Jungwirth, P. *J. Phys. Chem. B* **2005**, *109*, 7617−7623.

(65) Jungwirth, P.; Winter, B. *Annu. Rev. Phys. Chem.* **2008**, *59*, 343−366.

(66) Kudin, K. N.; Car, R. *J. Am. Chem. Soc.* **2008**, *130*, 3915−3919.

(67) Golub, G. H.; Loan, C. F. V. *Matrix Computations*; The Johns Hopkins University Press: Baltimore, MD, USA, 1996.

(68) Li, X.; Iyengar, S. S. *J. Chem. Phys.* **2010**, *133*, No. 184105.

(69) Swope, W. C.; Andersen, H. C.; Berens, P. H.; Wilson, K. R. *J. Chem. Phys.* **1982**, *76*, 637−649.

(70) Pulay, P. *Mol. Phys.* **1969**, *17*, 197−204.

(71) Goldstein, H.; Poole, C.; Safko, J. *Classical Mechanics*; Addison Wesley: San Francisco, CA, USA, 2002.

(72) Trotter, M. F. *Proc. Am. Math. Soc.* **1959**, *10*, 545−551.

(73) Nelson, E. *J. Math. Phys.* **1964**, *5*, 332−343.

(74) Czako, G.; Kaledin, A. L.; Bowman, J. M. *J. Chem. Phys.* **2010**, No. 132.

(75) Bowman, J. M.; Gazdy, B.; Sun, Q. Y. *J. Chem. Phys.* **1989**, *91* (5), 2859−2862.

(76) Miller, W. H.; Hase, W. L.; Darling, C. L. *J. Chem. Phys.* **1989**, *91*, 2863−2868.

(77) Riesz, F.; Sz.-Nagy, B. *Functional Analysis*; Dover: New York, 1990.

(78) Press, W. H.; Teukolsky, S. A.; Vetterling, W. T.; Flannery, B. P. *Numerical Recipes in C*; Cambridge University Press: New York, 1992.

(79) Fermi, E.; Pasta, J. R.; Ulam, S. Studies of non-linear problems. i. Technical Report No. 1940, Los Alamos Report, 1955.

(80) Robinson, P. J.; Holbrook, K. A. *Unimolecular Reactions*; John Wiley & Sons: New York., 1972.

(81) Forst, W. *Theory of Unimolecular Reactions*; Academic Press: New York, 1973.

(82) Jortner, J.; Levine, R. *Adv. Chem. Phys.* **1981**, *47* (Part 1), 1−114.

(83) Parmenter, C. S. *J. Phys. Chem.* **1982**, *86*, 1735−1750.

(84) Parmenter, C. S. *Faraday Discuss. Chem. Soc.* **1983**, *75*, 7−22.

(85) E. L. Sibert, I.; Reinhardt, W.; Hynes, J. *J. Chem. Phys.* **1984**, *82*, 1115−1134.

(86) Khundkar, L. R.; Zewail, A. H. *Annu. Rev. Phys. Chem.* **1990**, *41*, 15−60.

(87) Uzer, T.; Miller, W. H. *Phys. Rep.* **1991**, *199*, 73−146.

(88) Nesbitt, D. J.; Field, R. W. *J. Phys. Chem.* **1996**, *100*, 12735−12756.

(89) Gruebele, M. *Theor. Chem. Acc.* **2003**, *109*, 53−63.

(90) Liu, Y.; Lohr, L. L.; Barker, J. R. *J. Phys. Chem. B* **2005**, *109*, 8304−8309.

(91) Keshavamurthy, S. *Int. Rev. Phys. Chem.* **2007**, *26*, 521−584.

(92) Grocheng, K. *Constr. Approximation* **1993**, *9*, 283−297.

(93) Jacobsen, E.; Lyons, R. *IEEE Signal Process. Mag.* **2003**, *20*, 74−80.

(94) He, T. *J. Math. Anal. Appl.* **1998**, *224* (2), 182−200.

(95) Tolimieri, R.; An, M.; Lu, C. *Mathematics of Multidimensional Fourier Transform Algorithms*; Springer-Verlag: New York, 1993.

(96) Cohen-Tannoudji, C.; Diu, B.; Loloë, F. *Quantum Mechanics*, Vol. Ii; John Wiley & Sons: New York, 1977.

(97) (a) Locating and Estimating Air Emissions from Sources of 1,3-Butadiene, EPA-454/R-96-008; Office of Air Quality Planning and Standards, United States Environmental Protection Agency: Research Triangle Park, NC, USA, 1996. (b) Health Assessment of 1,3-Butadiene, EPA/600/P-98/001F; Office of Research and Development, United States Environmental Protection Agency: Washington, DC, 2002.

(98) Stevens, P. S.; Seymour, E. *J. Phys. Chem. A* **2000**, *104*, 5989−5997.

(99) Fan, J.; Zhang, R. *Environ. Chem.* **2004**, *1*, 140−149.

(100) Svozil, D.; Jungwirth, P. *J. Phys. Chem. A* **2006**, *110*, 9194−9199.

(101) Sadhukhan, S.; Munoz, D.; Adamo, C.; Scuseria, G. E. *Chem. Phys. Lett.* **1999**, *306*, 83−87.